



저작자표시-비영리-변경금지 2.0 대한민국

이용자는 아래의 조건을 따르는 경우에 한하여 자유롭게

- 이 저작물을 복제, 배포, 전송, 전시, 공연 및 방송할 수 있습니다.

다음과 같은 조건을 따라야 합니다:



저작자표시. 귀하는 원저작자를 표시하여야 합니다.



비영리. 귀하는 이 저작물을 영리 목적으로 이용할 수 없습니다.



변경금지. 귀하는 이 저작물을 개작, 변형 또는 가공할 수 없습니다.

- 귀하는, 이 저작물의 재이용이나 배포의 경우, 이 저작물에 적용된 이용허락조건을 명확하게 나타내어야 합니다.
- 저작권자로부터 별도의 허가를 받으면 이러한 조건들은 적용되지 않습니다.

저작권법에 따른 이용자의 권리는 위의 내용에 의하여 영향을 받지 않습니다.

이것은 [이용허락규약\(Legal Code\)](#)을 이해하기 쉽게 요약한 것입니다.

[Disclaimer](#)

**Master's Thesis of Science**

**Investigation of Ununiform Ship Phase Observed in  
High-Resolution TanDEM-X ATI-SAR using  
Electromagnetic Simulation**

**EM 시뮬레이터를 이용한 고해상도 TanDEM-X  
ATI-SAR에서 관찰된 선박의 불균일한 위상 조사**

**February 2020**

**Graduate School of Earth and Environmental Sciences  
Seoul National University**

**Seungchul Lee**

## Abstract

Ship speed monitoring is an essential component of sea traffic monitoring and disaster prevention. The Synthetic Aperture Radar (SAR) systems are suitable because they can be monitored regardless of the weather and time. Along-Track Interferometry SAR (ATI-SAR) is one of the Interferometric SAR (InSAR) technique that extract the surface velocity. Depending on the length of the Along-track, the speed can be measured using ATI data, from slower objects such as glaciers to faster objects such as ships. By increasing the resolution of the SAR data, an object can be observed in more detail. For example, the TerraSAR-X provides high-resolution SAR images using X-band, so a single object such as a ship can be observed in multiple pixels. With this data, we can measure the surface object velocity more accurately by using the ATI-SAR method. Therefore, the phase value of an object in ATI images must be the same because it indicates the speed of the object. However, some vessel speeds calculated as ATI-SAR results are different for each pixel. This is presumed to be caused by the ship's three-dimensional structure, acceleration and shaking. In a real environment, verifying these causes is not easy because various factors are reflected in the results.

In this study, we used an EM simulator to analyze the factors that could affect the ATI results. The simulator can reflect the three-dimensional characteristics of the object and add elements related to the movements that can occur in the ship. After that, two SAR images were calculated to produce ATI-SAR results. The simulated

SAR data have the same characteristics as the real SAR data; in addition, the results of the InSAR techniques XTI-SAR and ATI-SAR are confirmed to be the same as the theoretical values. Through this observation, various factors that may occur in the vessel are reflected in the InSAR results and are verified to affect the phase value. This was difficult to confirm directly with previous research methods.

The simulations can possibly be used for a variety of applications, including precise analysis of ATI-SAR results, system design of ATI-SAR satellites, and target identification and velocity extraction of artificial structures from InSAR outputs that include cross-track and along-track baselines.

**Keywords** – SAR, EM Simulator, ATI-SAR, Velocity estimation

**Student Number:** 2017-23937

# List of Contents

<b>Chapter 1. Introduction .....</b>	<b>- 1 -</b>
1.1 Study background .....	- 1 -
1.2 Purpose of research .....	- 2 -
<b>Chapter 2. Simulation design and data processing .....</b>	<b>- 4 -</b>
2.1 Electromagnetic (EM) simulator .....	- 4 -
2.1.1 Calculation method.....	- 9 -
2.1.2 CAD modeling .....	- 11 -
2.1.3 Stepped frequency .....	- 15 -
2.1.4 Simulation configuration .....	- 19 -
2.2 SAR focusing algorithms .....	- 25 -
2.2.1 Range direction focusing .....	- 25 -
2.2.2 Azimuth direction focusing .....	- 30 -
<b>Chapter 3. Simulation result.....</b>	<b>- 33 -</b>
3.1 Analysis of simulated SAR characteristics.....	- 37 -
3.1.1 Analysis of delay effect by the object.....	- 37 -
3.1.2 Analysis of structural characteristic by ship type.....	- 41 -
3.1.3 Analysis of rotation and polarization effect of ship.....	- 45 -
3.2 Result of XTI-SAR simulation .....	- 52 -
3.3 Result of ATI-SAR simulation .....	- 56 -
3.3.1 Extraction of object velocity surface velocity .....	- 56 -
3.3.2 ATI-SAR without cross-track baseline.....	- 59 -
3.3.3 ATI-SAR with cross-track baseline.....	- 63 -
3.3.4 Velocity extraction from ATI- and XTI-SAR.....	- 66 -

3.3.5	ATI-SAR results for moving ship .....	- 68 -
3.4	Analysis of phase error in Korean Strait .....	- 71 -
<b>Chapter 4.</b>	<b>Conclusions .....</b>	<b>- 75 -</b>
<b>Abstract in Korea.....</b>	<b>.....</b>	<b>- 77 -</b>
<b>Bibliography</b>	<b>-</b>	<b>79 -</b>

## List of figures

Figure 2-1 Flowchart of the SAR simulation.....	- 7 -
Figure 2-2 Interface of the Electromagnetic (EM) Simulator. ....	- 8 -
Figure 2-3 GTD-PO method of the sphere model. ....	- 10 -
Figure 2-4 Reference ship model and cross section of CAD model.....	- 13 -
Figure 2-5 GTD-PO method of the ship model. Red: GTD, Blue: PO.....	- 14 -
Figure 2-6 Stepped frequency signal in time-frequency domain .....	- 17 -
Figure 2-7 Geometry (left) and Schematic diagram (right) of the SAR simulation calculation process. ....	- 18 -
Figure 2-8 Illustration of the concept of synthetic aperture. ....	- 23 -
Figure 2-9 (a) Doppler frequency and (b) distance change relative to the $R_0$ in the azimuth direction. (Red: theoretical value, Blue: simulated value).....	- 24 -
Figure 2-10 High-resolution range profile of the sphere model.....	- 28 -
Figure 2-11 (a) Schematic of the phase wrapping environment. (b) Simulation results of the phase wrapping environment.....	- 29 -
Figure 2-12 (a) Range migration cell of the sphere model. (b) Projected coordinate system.....	- 32 -
Figure 3-1 Progress of SAR simulation.....	- 36 -
Figure 3-2 (a) Schematic of delay time difference between the antenna and target because of non-uniform structure of the ship (b) SAR simulation image reflecting delay time.....	- 39 -
Figure 3-3 (a) Simulated SAR image of the ship (b) TerraSAR-X SAR image of the ship. ....	- 40 -
Figure 3-4 (a), (c), and (e) - Reference ship models; (b), (d), and (f) – respective simulated SAR images of the ships. ....	- 44 -
Figure 3-5 Simulation overview of the rotation of the ship.....	- 47 -

Figure 3-6 HH polarized SAR simulation image for a rotating ship. ....	- 48 -
Figure 3-7 VH polarized SAR simulation image for a rotating ship. ....	- 49 -
Figure 3-8 HV polarized SAR simulation image for a rotating ship. ....	- 50 -
Figure 3-9 VV polarized SAR simulation image for a rotating ship. ....	- 51 -
Figure 3-10 Geometry of XTI-SAR simulation. ....	- 54 -
Figure 3-11 For $B_c = 80$ m, (a) DEM result of ship model, (b) flat-Earth DEM, and (c) corrected DEM values. For $B_c = 100$ m, (d) DEM result of ship model, (e) flat-Earth DEM, and (f) corrected DEM values. ....	- 55 -
Figure 3-12 Schematic geometry of the ATI-SAR simulation.....	- 58 -
Figure 3-13 ATI-SAR simulation overview of the moving ship. ....	- 61 -
Figure 3-14 Results of (a) $U_r = 0$ m/s (c) $U_r = -0.5$ m/s (e) $U_r = -1.0$ m/s ATI phase values. (b) $U_r = 0$ m/s (d) $U_r = -0.5$ m/s (f) $U_r = -1.0$ m/s calculated velocities.....	- 62 -
Figure 3-15 ATI-SAR simulation with cross-track baseline. ....	- 64 -
Figure 3-16 (a) $B_c = 0$ m (c) $B_c = 2$ m (e) $B_c = 10$ m (g) $B_c = 100$ m, ATI phase values. (b) $B_c = 0$ m (d) $B_c = 2$ m (f) $B_c = 10$ m (h) $B_c = 100$ m, calculated velocities.....	- 65 -
Figure 3-17 For a ship velocity of $-0.5$ m/s, (a) ATI-SAR result with cross-track baseline ( $BA = 150$ m, $BC = 10$ m), (b) residual phase (c)–(a), (c) ATI-SAR result ( $BA = 150$ m, $BC = 0$ m), (d) XTI-SAR result ( $BA = 0$ m, $BC = 10$ m), and (e) adjusted ATI-SAR results of (a)–(d).....	- 67 -
Figure 3-18 Simulation overview of the ship movement.....	- 69 -
Figure 3-19 (a) Simulation SAR results; velocity extraction results using ATI-SAR when $b, T_z = 0$ m/s (c) $T_z = 0.1$ m/s and (d) $T_z = -0.1$ m/s.....	- 70 -
Figure 3-20 (a) TanDEM-X perpendicular and (b) along-track baseline for different latitudes for the bistatic short baseline phase from June 10, 2011 to August 16, 2012. Velocity error value depending on latitude when height difference is (c) 0 m, (d) 10 m, and (e) 30 m. ....	- 74 -

## List of Tables

Table 3-1 Parameters for EM simulation.....	- 35 -
Table 3-2 Specification of Ships used in Simulation .....	- 43 -
Table 3-3 Perpendicular baseline of Korean Strait in TanDEM-X. ....	- 73 -

# **Chapter 1.**

## **Introduction**

### **1.1 Study background**

The Interferometric Synthetic Aperture Radar (InSAR) is a technique used for extracting surface information by obtaining phase difference using the data from two or more Single Look Complex (SLC) SAR image. Along-Track Interferometry (ATI) is a system that uses the phase difference caused by the geometric difference of two signals obtained with a short time interval. The two SAR antennas are moved to the same orbit (or back and forth on the same platform) at short distances to transmit and receive signals to obtain the required data. After the SAR data are acquired from each antenna, an interferogram image of the two data sets is generated from which the speed of the moving object on the surface can be measured. These systems are mainly used in airborne SAR systems. In spaceborne systems, the Shuttle Radar Topography Mission (SRTM) and the TerraSAR-X support the ATI mode.

Compared to SRTM, the TerraSAR-X has a higher instrument noise level and a shorter follow-track baseline. Moreover, a higher pixel resolution permits more spatial averaging for the same effective resolution. TerraSAR-X simulations assumed that the effective along-track baseline is short. and that the backscattering characteristics of the water surface are homogeneous. Consequently, the images remain unaffected by the strong artifacts associated with azimuth ambiguities, for

example, ghost images of nearby regions of increased backscatter in regions of low backscatter (Romeiser, Suchandt et al. 2010).

As a result, both satellites act as a large single-pass radar interferometer with the opportunity for a flexible baseline selection. This enables the acquisition of highly accurate cross-track and along-track baseline interferograms without the inherent accuracy limitations imposed by the repeat-pass interferometry because of the temporal decorrelation and the atmospheric disturbances (Hanssen 2001). In addition to the primary goal of the mission, several secondary mission objectives based on ATI, such as polarimetric SAR interferometry (PolInSAR), digital beamforming, and bistatic radar have been defined, which represents an important and innovative asset of the mission. Using these features, studies are actively conducted using TerraSAR-X ATI data for analyzing ocean currents(Kim, Moon et al. 2003), river speed monitoring, traffic congestion monitoring, and ship tracking at sea. (Kim, Moon et al. 2003, Meyer, Hinz et al. 2007, Kim, Jung et al. 2015, Kim and Kim 2017, Kang and Kim 2019)

## **1.2 Purpose of research**

In high resolution ATI-SAR data, the object's phase values are heterogeneous. Moreover, incorrect phase values not only cause object velocity errors, but also reduce the reliability of the entire image. To extract the velocity of an object in a heterogeneous InSAR phase, we need to consider other factors that affect the InSAR

result. For example, the rotation of an object or its movement caused by waves can affect the InSAR results. TanDEM-X particularly follows a double helix orbit which generates a cross-baseline and an along-track baseline. Thus, both ATI and XTI systems can be used for the obtaining the data; however, longer along-track base lines inevitably include the cross-track baselines. Previous ATI studies using TanDEM-X had omitted this cross-track component(Krieger, Moreira et al. 2007) because it can cause an additional phase value when the target has non-uniform heights. However, in the real world, it is difficult to verify these assumptions because various factors should be considered.

This study aims to simulate InSAR and analyze the factors that influence the InSAR results. To analyze factors such as possible movements of objects in a controlled environment, we conducted experiments using the electromagnetic simulator and analyzed their result.

The outline of the rest of paper is as follows. Chapter 2 introduces the concept of electromagnetic simulator and the parameters required for designing the simulation. The characteristics of the SAR images obtained from the simulation and the results of the InSAR study are derived in Chapter 3. Finally, Chapter 4 states the conclusion of the study.

## **Chapter 2.**

### **Simulation design and data processing**

The progress of this study is shown in Figure 2-1. This chapter will explain the overall concept of the electromagnetic simulator and the parameters required for its simulation. In addition, it describes an algorithm that focuses on raw data and extracts velocity using simulation SAR image.

#### **2.1 Electromagnetic (EM) simulator**

The design of devices, such as the satellite radar, mobile phones, and radios, that use electromagnetic waves involves intricate systems that use antennas and is quite complex. As a result, there are multiple factors to be considered while designing system; thus, it is difficult to measure the effectiveness and accuracy of these systems. Therefore, to facilitate the design and testing of electromagnetic systems assisted design and simulation tools are used to model the electromagnetic system, to introduce the parameters that define it, and to simulate its operation. Moreover, significant amounts of time and money can be saved owing to the ease of changing the system parameters using the EM software tool, and because such tests are not performed using any materials.

To analyze the scattering characteristics of the three-dimensional structure of the

object, we used Computer Aided Design (CAD) data to describe the object in the simulation. Previous studies using EM solvers with CAD have been used primarily for the identification and classification of the targets, for example, ship classification (Menon, Boudreau et al. 1993) and iceberg tracking (Ferdous, McGuire et al. 2018). In addition, previous studies primarily relied the Inverse Synthetic Aperture Radar (ISAR) method for creating the SAR images through EM simulation. ISAR is used for scenarios where the radar is stationary, and the targets are in motion. This has the same situation as a spotlight SAR which the radar moves along a circular flight path (Ozdemir 2012). This is because most EM simulators provide SAR simulation using ISAR which is more suitable for calculating the Radar Cross Section (RCS) related to object identification (Kim, Seo et al. 2005).

However, the ISAR method that employs the circular coordinate system causes inconvenience while setting the elements such as the speed and rotation of the object. Therefore, in this study, we used a software, newFasant that can perform simulations using the Cartesian coordinate system. Both the antenna and the object can move freely in the Cartesian coordinate system.

The EM Simulator used in the study, newFasant, was created by a research group at the University of Alcalá de Henares in 1995 (Romero 2010). In November 2010, a technology-based company NewFasant S.L (Timoteo 2011) was established, which was led by the same research group. Moreover, the company developed a software tool, newFASANT, a simulation tool for electromagnetic field analysis that offers a variety of simulation possibilities. In fact, the tool consists of several products (also

called "modules"), which are responsible for different tasks, and are classified according to whether they are used in the RCS or in antenna calculations. The module used in this study automatically combines the radio frequency technologies in Geometrical Theory of Diffraction (GTD) and Physical Optics (PO) for the RCS analysis of complex objects (airplanes, satellites, ground vehicles, ships, etc.) with antennas and radio waves in metropolitan environments. This module is labeled GTD-PO as shown in Figure 2-2. The different parts of the scenario are categorized for analysis using the GTD or PO according to their geometric characteristics and simulation parameters, which provides an excellent combination of efficiency and accuracy (García Díaz 2015).

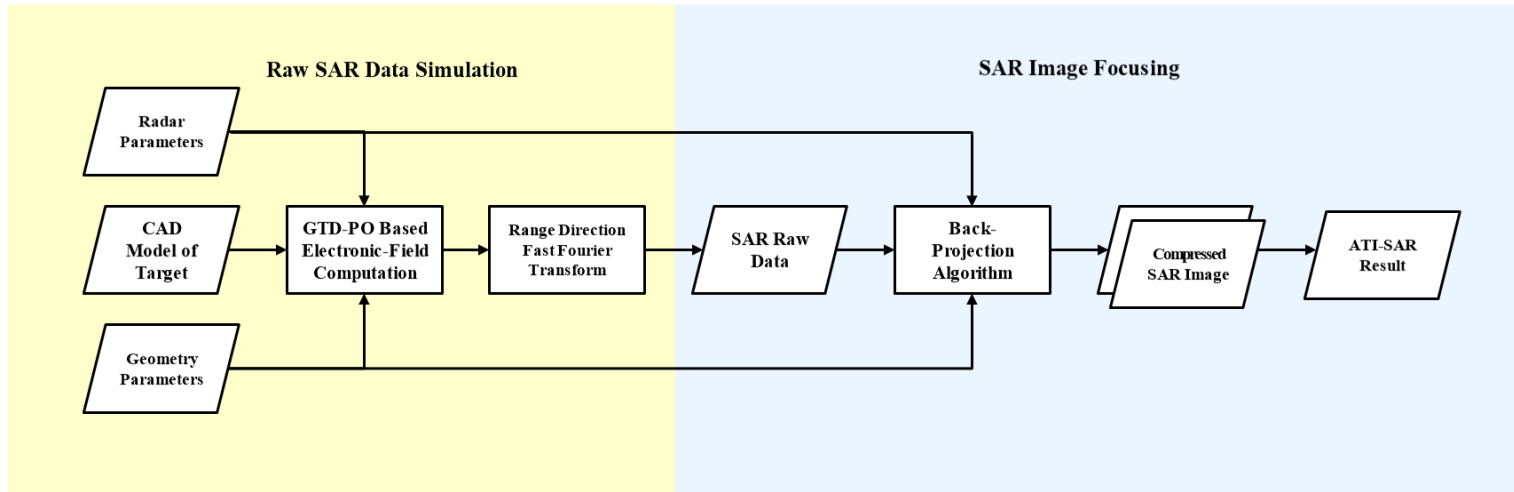
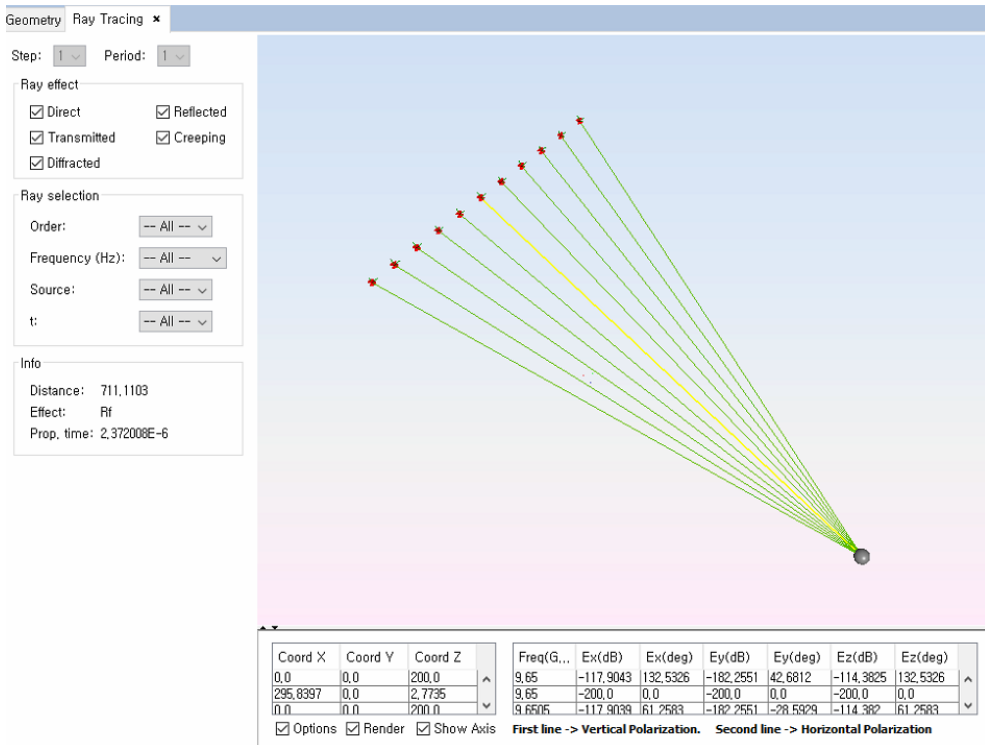


Figure 2-1 Flowchart of the SAR simulation.



**Figure 2-2 Interface of the Electromagnetic (EM) Simulator.**

### **2.1.1 Calculation method**

The actual size of artificial targets, such as ships, is too large for numerical solutions. Although the EM simulator supports the method of calculating the moment of the scattering, its practical implementation is impossible because it consumes considerable memory and time. Therefore, the PO method with multiple bounces was considered as the best fit for the current task. The PO replaces surfaces with small triangular facets such that the dimension of these are an order less than the wavelength of the central frequency as depicted in Figure 2-3. (Moreno, Caballero et al. 2013). Furthermore, GTD is an extension of geometrical optics which accounts for diffraction. It introduces diffracted rays in addition to those usually employed in geometrical optics. These rays are produced by incident rays that hit the edges, corners, and vertices of the boundary surfaces or by those which graze such surfaces (Keller 1962).

In PO and hybrid GTD-PO solutions all the surfaces in the problems are analyzed considering the frequency and their distances from the source: the surfaces that satisfy the GTD premises are analyzed using GTD; whereas, the PO is employed for other surfaces. The combined method is more accurate than GTD alone and more efficient compared to using just the PO. In addition, it permits the phase analysis. Because structures like spheres have a large curvature, many triangular facets are required to calculate PO. Therefore, the GTD method is advantageous in this calculation.

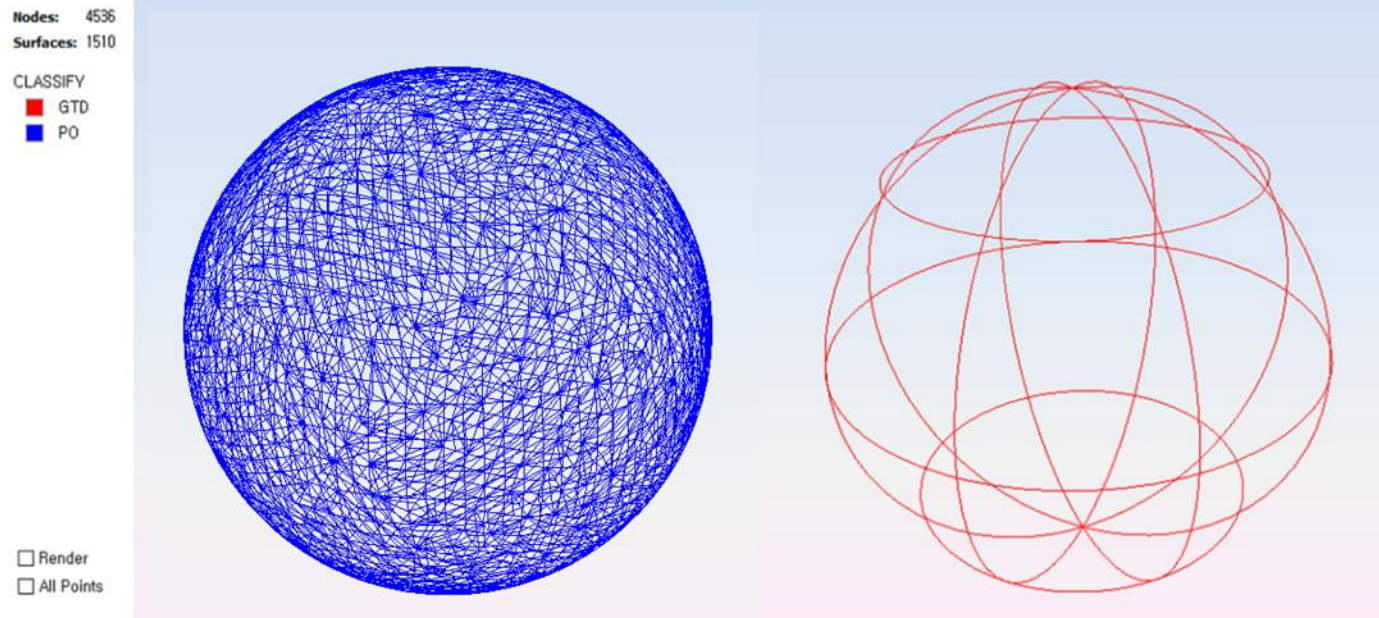


**Figure 2-3 GTD-PO method of the sphere model.**

### **2.1.2 CAD modeling**

A simulation employing the EM simulator can analyze the scattering characteristics of an object using the electromagnetic waves. To do this, we need to create a CAD model that simulates the object.

The actual vessel was digitally modeled as a reference, as shown in Figure 2-4. A simulation of the object in as much detail as possible would be preferred; moreover, it would require a considerable amount of resources for its calculation. Therefore, to create a CAD model that reflected the characteristics of the object using minimal calculation, the characteristic structures that significantly affect the scattering characteristics of the electromagnetic waves were elaborately expressed; whereas the structures that have relatively less influence been expressed in a simple manner as below Figure 2-5.

In newFasant, the materials can be assigned to each part of the CAD model and are reflected in the calculations (Moreno, Caballero et al. 2013). The permittivity of a material is an index of the amount of electricity generated in a medium when electromagnetic waves enter the material. The materials considered here had different permittivity. Metals with high conductivity are called conductors and have several free electrons inside them which are not bound strongly to the nuclei of the atoms. When the electromagnetic waves enter a material, currents are induced by promoting the motion of free electrons. Scattering is the process by which the movement of these energized free electrons radiates a different electric field. Radar is a sensor that

receives these re-radiated microwaves and uses these received signals to measure the electrical characteristics of the object under observation. Consequently, a metal having a high permittivity has more free electrons; thus, it re-radiates a microwave that has a larger amplitude, thereby emitting a stronger signal for the radar to receive (Ishimaru 1978).

Because ships are generally made of steel, this study assumes that they have a 100% permittivity. However, there are some non-metal parts and the metal are coated with paint to prevent corrosion. Considering these factors, the next study was carried out by applying these properties of the materials to each part.

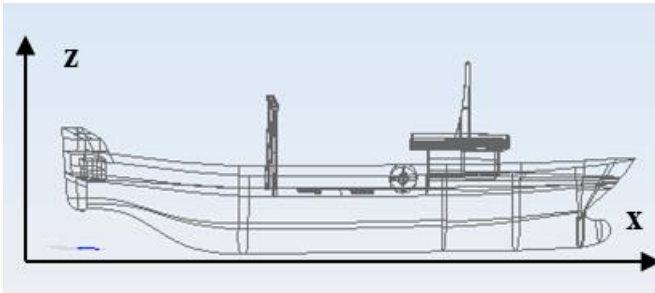


**Figure 2-4 Reference ship model and cross section of CAD model**

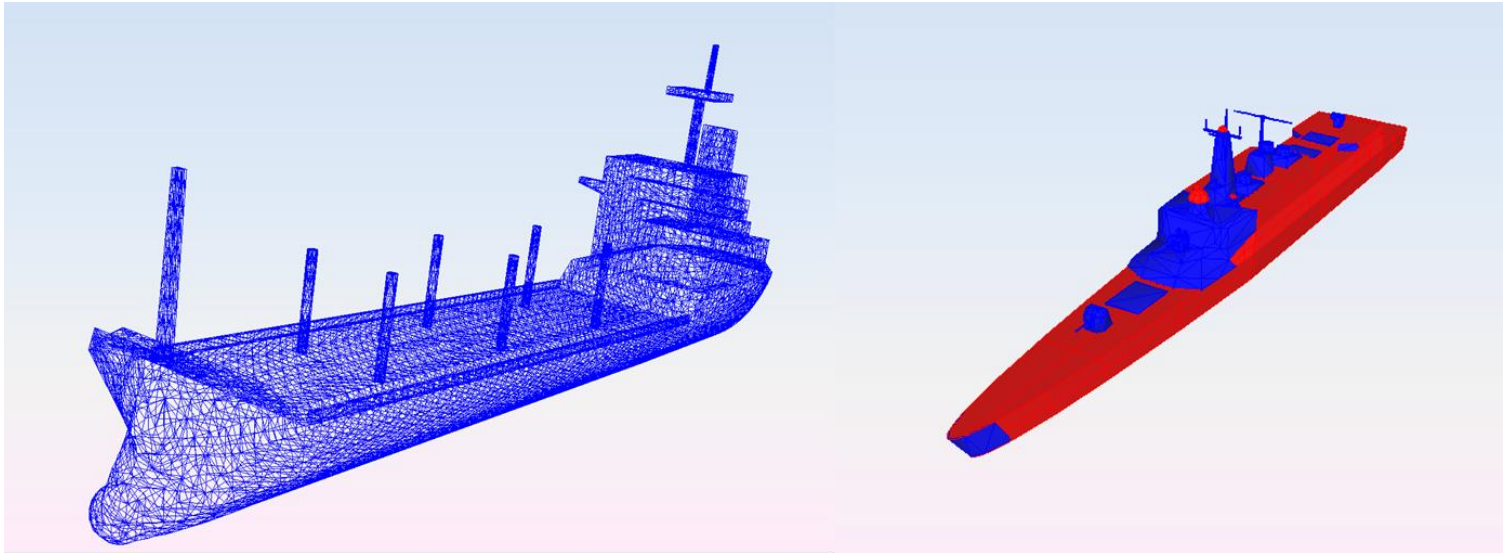


**Figure 2-5 GTD-PO method of the ship model. Red: GTD, Blue: PO**

### 2.1.3 Stepped frequency

Stepped frequency radar is one of the popular radar waveform, this radar composed of pulse compression like a chirp signal, where the carrier frequency of the continuous pulse is varied by a fixed frequency step  $\Delta f$ . This technology increases the bandwidth by using multiple pulses. Moreover, it exploits the equivalence between time and frequency domain representations of a target response to obtain the scattering characterization of a target from its frequency response. Instead of collecting the range profile directly in the time domain, the frequency response of the target is collected over a finite bandwidth by switching the frequency of the Radiofrequency pulse at a pulse-to-pulse rate.

Stepped frequency is formed by emitting a series of single-frequency short continuous subwaves. In generating the stepped frequency signal, the frequencies between adjacent subwaves are increased by an incremental frequency of  $\Delta f$  as demonstrated in Figure 2-6. Stepped frequency signal has a discrete frequency. Each subwave has a Pulse Duration Interval (PRI). The total frequency Bandwidth (BW) expressed as the product of the coherent integrated pulse number  $N$  and the frequency step size  $\Delta f$ .

$$BW = (f_n - f_1) + \Delta f = N \cdot \Delta f \quad (1)$$

Center frequency of the radar,  $f_c$ , and the frequency increment (or resolution),  $\Delta f$ , can be calculated as below:

$$\Delta f = f_n - f_{n-1} = \frac{BW}{N} \quad (2)$$

$$f_c = \frac{f_1 + f_n}{2} \quad (3)$$

The stepped frequency signal for SAR can be used to estimate the range of a possible target in the following Eq. (4):

$$S(f)_{if} = \int_{t_1}^{t_i} \int_{f_0}^{f_{N-1}} E_s(f(x_i, y_i, z_i), U(X_i, Y_i, Z_i), f, t_i) \cdot e^{-2jkR_i} df dt \quad (4)$$

The electric field,  $E_s$ , is affected by the distance,  $R$ , between the target and the radar. Suppose that the target  $f(x, y, z)$  is in  $R$  from the radar  $U(X, Y, Z)$ . The phase  $e^{-2jkR}$  of the received wave is proportional to the distance, and  $k$  is the wavenumber vector corresponding to the stepped frequency vector of  $f = [f_0, f_2 \dots f_{N-1}]$  (Ozdemir 2012). As shown in Figure 2-7,  $t$  is the slow time, which is the time the antenna travels. Assume that the interval time,  $\Delta t$ , for slow time is equal to the Pulse Repetition Interval (PRI).

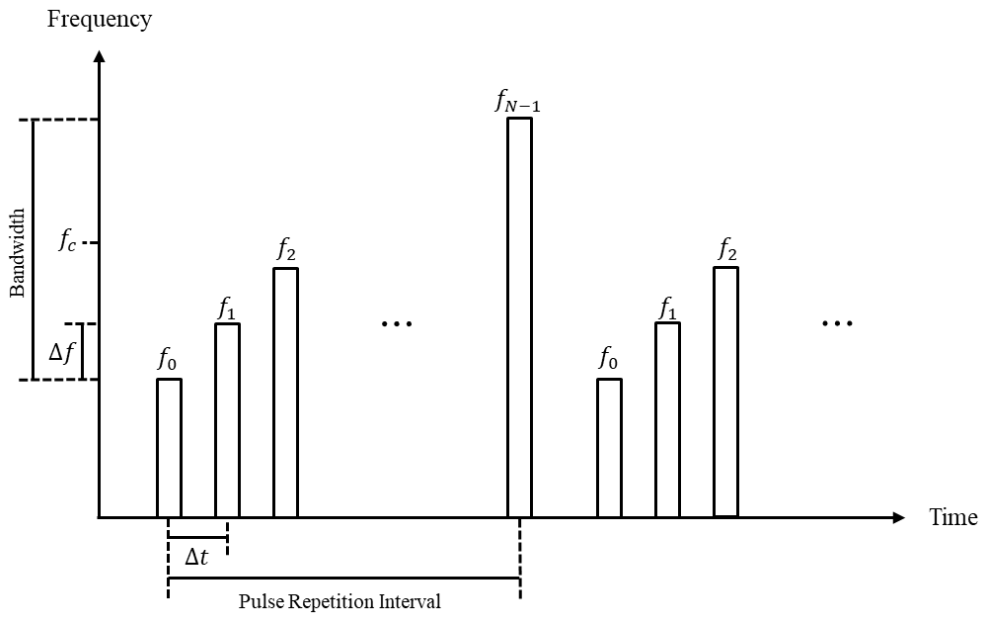


**Figure 2-6 Stepped frequency signal in time-frequency domain**

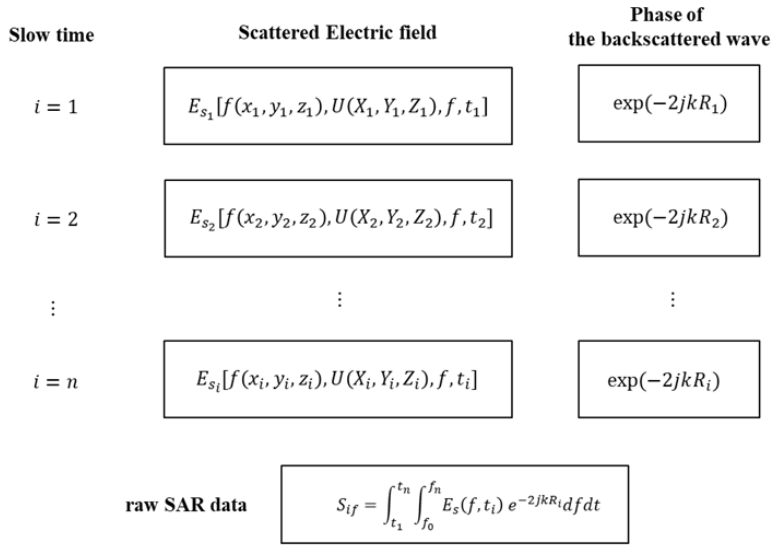
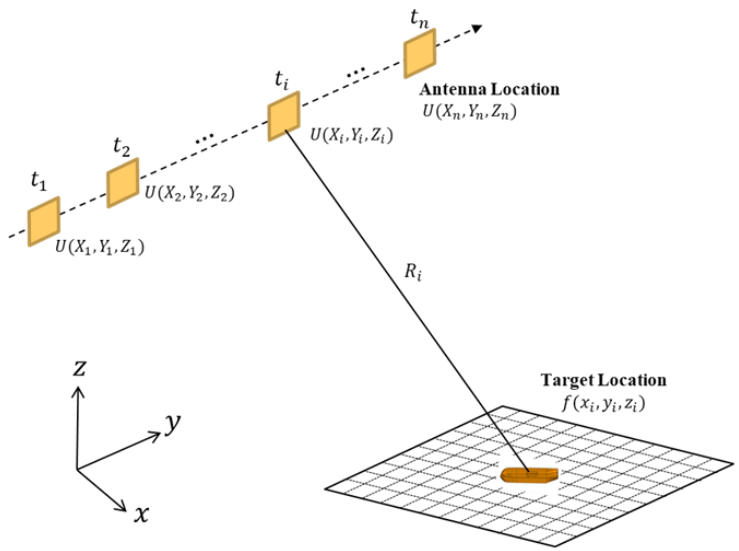


Figure 2-7 Geometry (left) and Schematic diagram (right) of the SAR simulation calculation process.

### 2.1.4 Simulation configuration

While designing a simulation, it is important to have a good understanding of the SAR and the characteristics of the simulator. In addition, because the performance of the system is limited, it must be considered while creating the simulation environment.

While setting the pulse repetition frequency (PRF) in a simulation, the Nyquist sampling rate should be considered. The PRF should be larger than the azimuth signal bandwidth because it corresponds to a complex sampler. If the PRF is too low, azimuth ambiguities caused by aliasing will problems. The azimuth oversampling ratio is usually higher than the range oversampling ratio because the azimuth spectrum rolls off slower than the range spectrum (Cumming and Wong 2005). Therefore, it is necessary to construct an optimal PRF that does not cause ambiguity. PRF is the inverse of PRI, the time interval in the azimuth direction.

$$\text{PRF} = \frac{1}{\text{PRI}} = \frac{1}{\Delta t} \quad (5)$$

The distance  $U(Y_t)$ , in which the antenna moves in the y direction in time  $t$ , can be defined as in Eq. (6) below.

$$U(Y_t) = V_s \times t \quad (6)$$

where,  $V_s$  is the speed of the platform.

When the shortest distance between the target and the platform is  $R_0$ , as shown in the Figure 2-8 below, the value of the distance  $R(t)$  between the platform and the target is given by Eq. (7).

$$R(t) = \sqrt{R_0^2 + U(Y_t)^2} \quad (7)$$

To avoid ambiguity in the azimuth, the distance covered by the antenna during the time interval  $\Delta t$  should be less than half of the wavelength. Therefore, while configuring the experimental environment, a PRF that satisfies this condition, as given by Eq. (8), was set.

$$R(t) - R(t - \Delta t) < \frac{\lambda}{2} \quad (8)$$

The azimuth resolution is given by the azimuth beam width. This beam width is determined by the radar wavelength  $\lambda$  and the antenna length  $L_a$ . Both these parameters are fixed for a given radar system (Cumming and Wong 2005).

Using these parameters, we can calculate the Synthetic Aperture Length,  $L_s$ , using Eq. (9).

$$L_s = \frac{0.886 R_0 \lambda V_s}{L_a \cos\theta_{r,c} V_g} \quad (9)$$

Here,  $\theta_{r,c}$  is the squint angle of the antenna, and  $V_g$  is the speed of the surface, which may be different from the platform speed  $V_s$  because the earth is spherical. However, the difference between them is negligible; therefore, this study assumes that  $V_s$  and  $V_g$  have the same values.

To verify the ambiguity of the Doppler frequency in the direction of azimuth in the simulation, we experimented as shown in Figure 2-9 below. The  $L_s$  used in the experiment is 2,500 m and the wavelength is 0.003 m. PRI is  $10^{-8}$ s, which satisfies the condition of Eq (8). The phase according to the distance that changes as  $t_i$  increases may be expressed as in Eq. (10) below.

$$S(f)_{if} = \int_{t_1}^{t_i} e^{-2jkR_i} dt \quad (10)$$

The red line in Figure 2-9 (b) shows the difference in distance from  $R_0$ . Using this, phase value was created using Eq. (10) as shown in Figure. 2-9 (a). The blue line in Figure. 2-9 (a) is the phase value obtained by using the EM simulator. The result of converting this to distance is shown in Figure 2-9 (b). Although the amplitude values

in Figure (a) are somewhat different between the theoretical and simulated values, the distance values in Figure (b) are almost identical. This confirms that there is no ambiguity of Doppler frequency in the direction of azimuth.

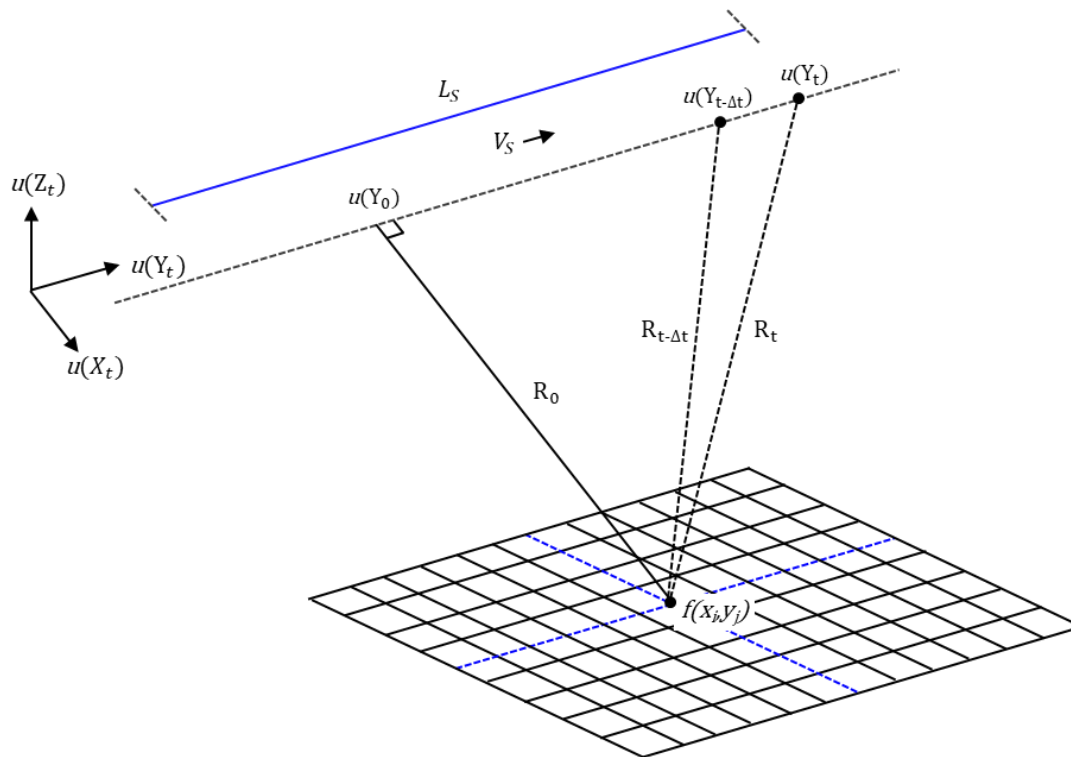


**Figure 2-8 Illustration of the concept of synthetic aperture.**

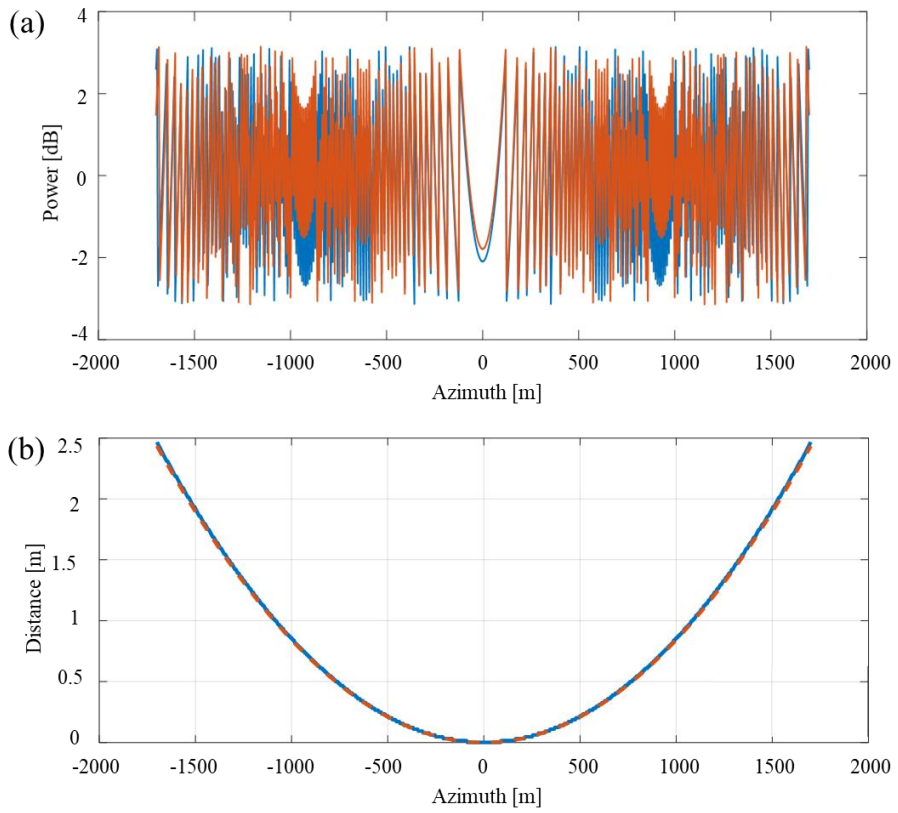


**Figure 2-9 (a) Doppler frequency and (b) distance change relative to the  $R_0$  in the azimuth direction. (Red: theoretical value, Blue: simulated value)**

## 2.2 SAR focusing algorithms

### 2.2.1 Range direction focusing

Since the simulation results are in the frequency domain, an inverse Fourier transform (IFT) should be used to convert these results into the time domain. The IFT can synthesize a frequency-domain signal from its spectrum of frequency components to its time-domain form. For a continuous signal  $S(f)$ , where  $-\infty < f < \infty$ , the IFT is described as

$$s(t) = \mathcal{F}^{-1}\{S(f)\} = \int_{-\infty}^{\infty} S(f)e^{j2\pi ft} df \quad (11)$$

The returns of the  $N$  pulses at different carrier frequencies form the frequency spectrum of the target reflectivity and are coherently integrated by the inverse fast Fourier transform (IFFT) to give the high-resolution range (HRR) profile as shown in Figure 2-10.

$$IFFT_{range}S_{IF}(\Delta f, N) = S_{IF}(\tau, N) \quad (12)$$

The resolution in the time domain is related to the inverse of the bandwidth in the frequency domain.

$$\Delta R = \frac{c}{2BW} \quad (13)$$

Where,  $c$  is speed of light.

Moreover, the maximum observable range  $R_{max}$  in the simulation is proportional to the number of samples  $N$ .

$$R_{max} = \Delta R \times N \quad (14)$$

As given by Eq. (14), the larger the number of samples  $N$  is the farther away the object under observation can be. However, since a large amount of computer resources are required, the sample size is generally set by considering the object size. Observing an object outside  $R_{max}$  creates ambiguity, which further causes phase wrapping. If the phase information is incorrect, as in this case, the resultant target information may provide a miscalculated distance of the object from the radar.

In this experiment, because no other object was considered between the antenna and the target, the phase wrapping was tested using Eq. (15), which verifies that  $R_{max}$  is wrapped  $N_{wrap}$  times.

$$R = R_{max} \times N_{wrap} + R_{rest} \quad (15)$$

where  $R$  is the distance between the actual target and the antenna and  $R_{rest}$  is the remainder of  $R$ .

Figure 2-11 (a) shows the simulation for  $R = 900$  m,  $\Delta R = 0.991$  m, and  $N = 200$ . Using Eq. (15),  $R_{rest}$  was calculated as 107.2 m. The simulation result is 106.9 m as depicted in Figure 2-11 (b), which is within the error range of  $\Delta R$ . This simulation required accurate estimates of the positions and magnitudes of the scattering center on the target.

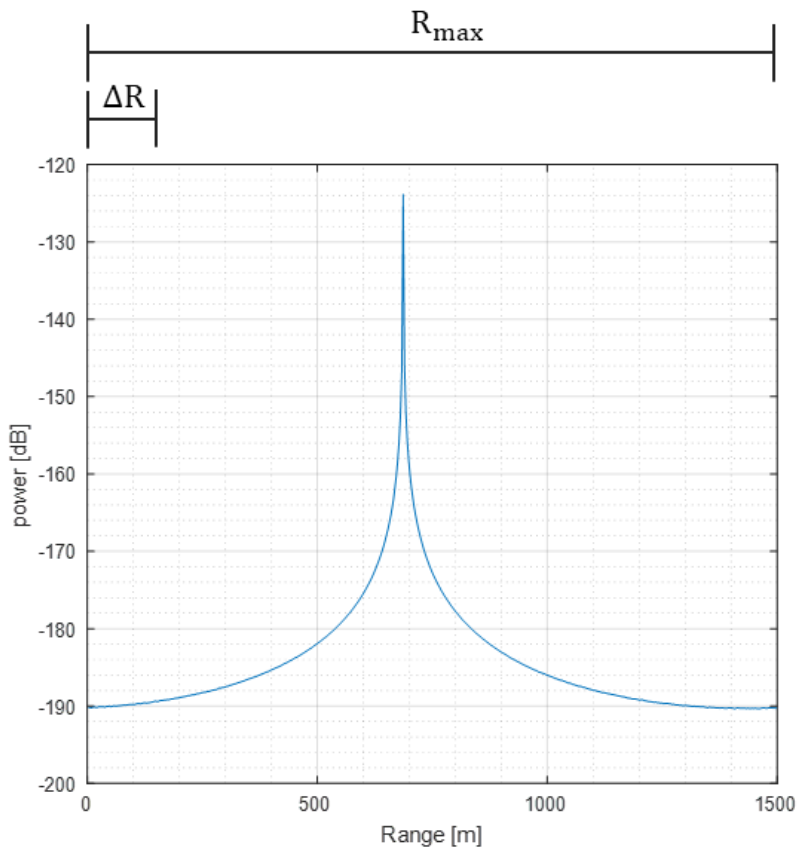


**Figure 2-10 High-resolution range profile of the sphere model.**

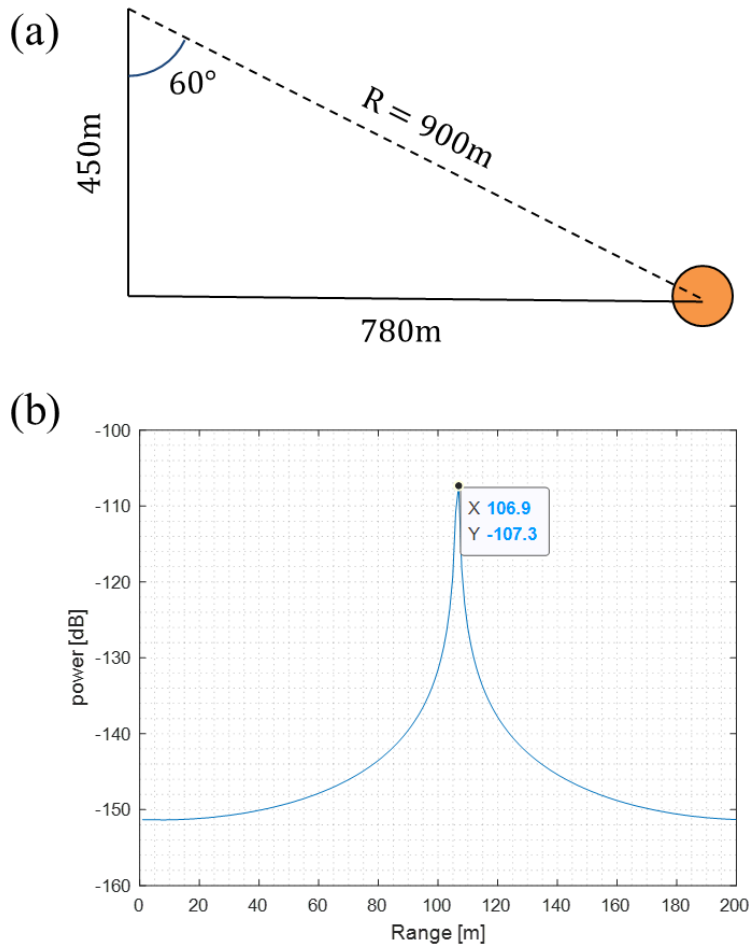


**Figure 2-11 (a) Schematic of the phase wrapping environment. (b) Simulation results of the phase wrapping environment.**

### 2.2.2 Azimuth direction focusing

The compression of SAR raw data can be performed using a variety of algorithms such as the Range Doppler Algorithm (RDA), the Frequency Scaling Algorithm (FSA), and the  $\Omega$ -k algorithm (Cumming and Wong 2005).

Generally, in the frequency domain, the image restoration algorithm is performed because it provides an easy calculation of the convolution. The impulse response grows longer as the distance between the target and the antenna increases. This results in a range cell migration curve. To use discrete Fourier transform (DFT) to change this image in the frequency domain, Range Cell Migration Correction (RCMC) is used to align the impulse response back to the same position. However, RCMC uses an approximation which leads to errors.

On the other hand, the Back-Projection Algorithm (BPA) is a method that reconstructs images in the time domain instead of the frequency domain (Nguyen, Ressler et al. 2004). It is used in topography and Magnetic resonance imaging.

In the simulation, the exact geometric location of the target relative to the antenna is known; therefore, we employed the BPA for image focusing. The relation between the time,  $t_d$ , between the pixels  $(x_i, y_j)$  in the coordinate system, where the image is projected, and the position of the antennas  $(u_m)$  c

an be expressed as follows (Soumekh 1999):

$$t_d = \frac{2}{c} \sqrt{x_i^2 + (y_j - u_m)^2} \quad (16)$$

Using the distance  $R_d(t, \eta)$ , we found the signal in the RCM image and added all the signals to the pixel  $(x_i, y_j)$ , as shown in Figure 2-12. The conjugate of the convolution with the reference signal,  $S_0^*$ , removes the phase corresponding to the distance component, as given by Eqs. (17) and (18).

$$\sum_y \sum_x \sum_m S_{IF}(t_d, u_m) \times S_0^*(t_d, u_m) \quad (17)$$

$$S_0^*(\tau_d, \eta) = \exp \left\{ -j2\pi \left( \frac{2R_d}{\lambda} \right) \right\} \quad (18)$$

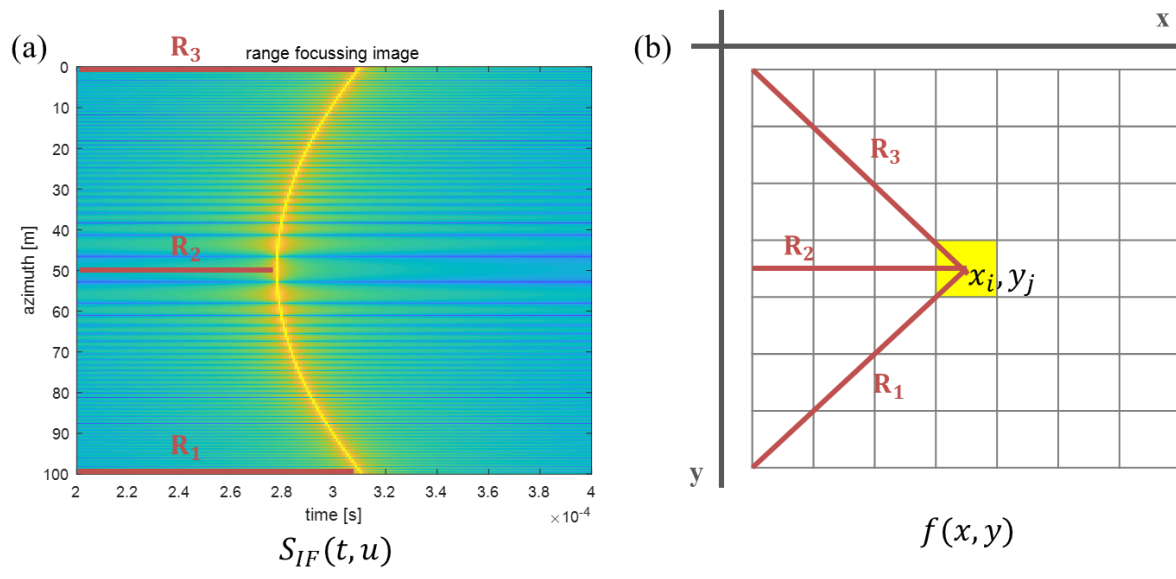


Figure 2-12 (a) Range migration cell of the sphere model. (b) Projected coordinate system.

## **Chapter 3.**

### **Simulation result**

We created the raw SAR data for the ship model through simulation. To create a TerraSAR-X like environment, the parameters we used are provided in Table 3-1. In the implementation of the GTD-PO model, the complex part of the object uses the PO model whereas the simple part utilizes the GTD model.

The result of simulation calculations is the same as that provided in Figure 3-1. It has a strong amplitude value when the antenna is the closest to the object. The range profile calculated using the IDFT is also depicted in the figure. Moreover, this range profile shows that if the distance between the object and the antenna is long, the impulse response is delayed.

The calculation of electromagnetic waves using CAD in the EM solver requires a considerable computation in proportion to the size of the object; this not only high-performance CPU, but also a considerable amount of memory. The CPU used in the experiment was the Intel® Core™ i7-7820X @ 3.60 GHz with 128 GB RAM, SSD with 500 GB storage, and the Windows 10 64-bit operating system.

The image formed by the EM simulator can be restored by using the distance between the pixels of the coordinate system in which the image is projected and the position of the antenna. The reconstructed image is depicted in the figure.

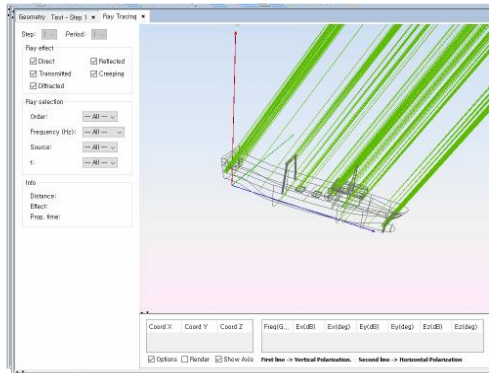
The image reflected the scattering characteristics of the selected object by using the

GTD-PO method. Interestingly, only a part of the ship emits strong amplitude signals; this is a result of the object's non-uniform structure which causes some parts of it to reflect more than the others.

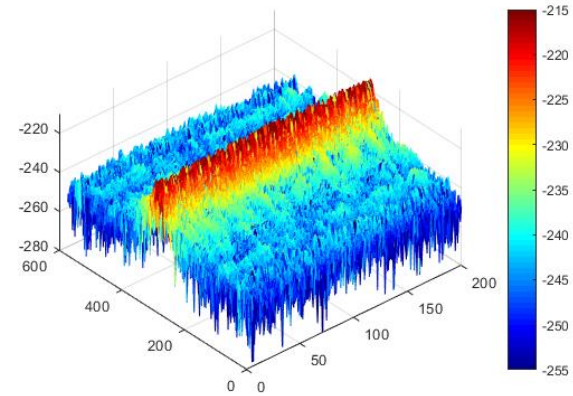
**Table 3-1 Parameters for EM simulation**

<b>Name</b>	<b>Value</b>	<b>Additional information</b>
Platform Velocity	7500m/s	Azimuth Direction
Along Track Baseline	150m	
PRI	$4 \times 10^{-4}$ s	
Azimuth Length	-1750m~1750m	
Azimuth Sample	1151	
Range Resolution	1m	
Azimuth Resolution	3m	
Center Frequency	9.65 Ghz	X band
Bandwidth	150 Mhz	
Incidence Angle	30°	

## Setup the Simulation



## Calculated Simulation Data



Electronic-Field  
Computation



Range Direction  
Fast Fourier Transform



## SAR raw Data

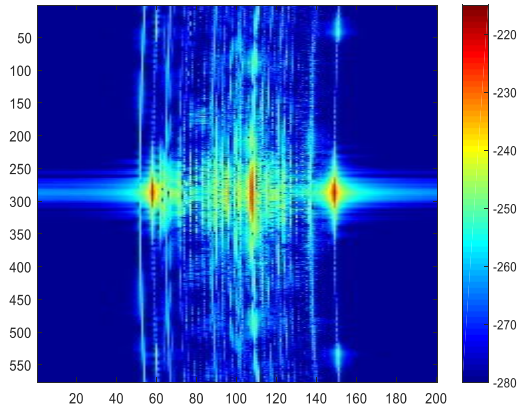


Image Focusing  
Algorithm



## Compressed SAR image

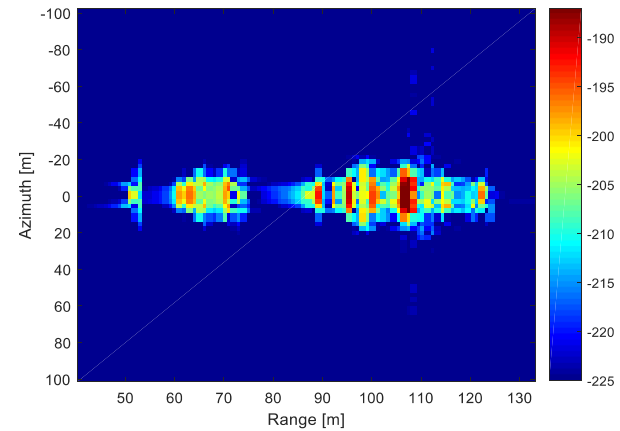


Figure 3-1 Progress of SAR simulation.

## 3.1 Analysis of simulated SAR characteristics

### 3.1.1 Analysis of delay effect by the object

The SAR image is obtained by transmitting electromagnetic waves which are reflected from the object surface and are received back. As a result, for the same object, the SAR image may vary depending on the squint angle, permittivity, rotation of the object, and other such factors. We examined whether the SAR image obtained by the simulator reflects these characteristics of the electromagnetic waves.

The distance  $R(\tau)$  of the object can be calculated using Eq. (19) through the delay between the times when the EM waves are reflected from the object and from the ground. In this case, the object is higher than the ground, as shown in Figure 3-2 (a). Therefore, the EM waves will reflect off before reaching the ground and will have a shorter delay. Moreover, the position of the object in the image will change according to the height of the object  $z$  and incidence angle  $\theta_{inc}$  in the reconstructed SAR image. This can be expressed using Eq. (20) when the value of  $R(\tau)$  is much longer than  $z$ .

$$R(\tau) = \tau \times c \quad (19)$$

$$R(\tau)_{obj} = R(\tau) - z \cos\theta_{inc} \quad (20)$$

This characteristic is also visible in the simulation results. In Figure 3-2(a), the SAR image depicts that the antenna in front of the ship has moved forward. The height of the antenna is 20.9 m from the ground, and the height of the vessel is 7.8 m. Calculating using the above equation, the time delay was approximately 3.78 s from the head, which would result in an offset of 11.4 m from the vessel. Checking this with the simulation image in Figure 3-2 (b), an offset of approximately 11 m had occurred relative to the position of the ship.

Figure 3-3 shows a comparison of the data obtained from the actual TerraSAR-X ship and from the simulation. The steering room located at the stern has shifted relative to the location of rest of the ship in the simulation.

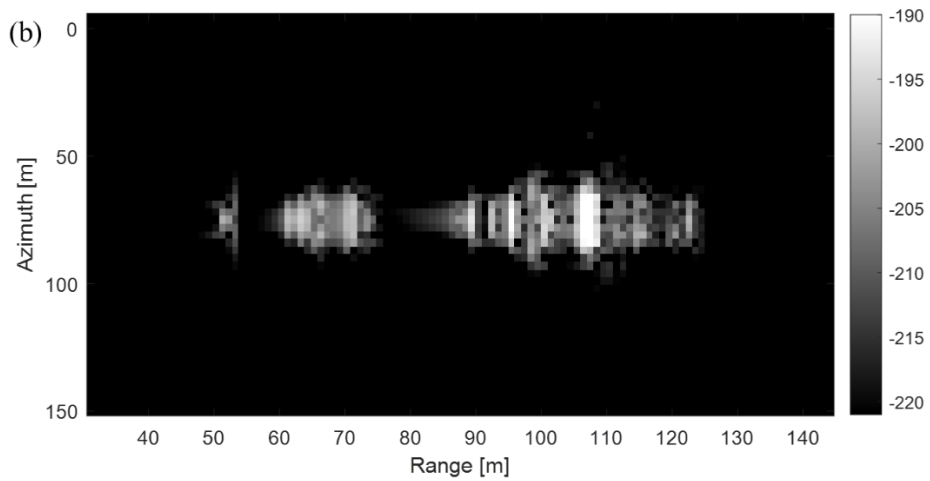
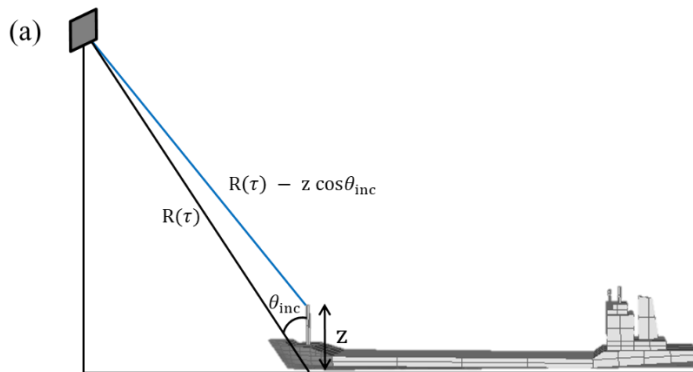


**Figure 3-2 (a) Schematic of delay time difference between the antenna and target because of non-uniform structure of the ship (b) SAR simulation image reflecting delay time.**

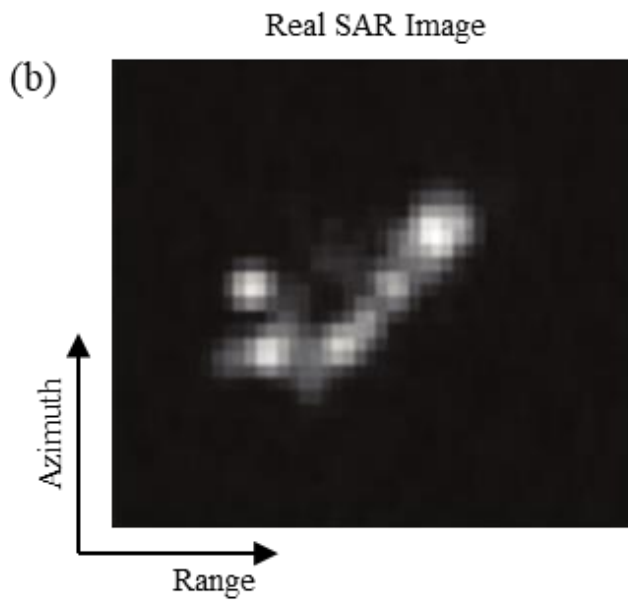
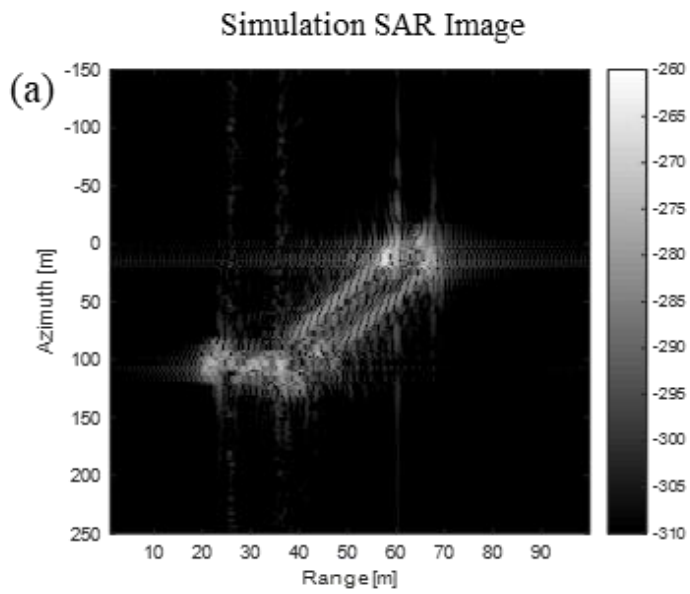


Figure 3-3 (a) Simulated SAR image of the ship (b) TerraSAR-X SAR image of the ship.

### **3.1.2 Analysis of structural characteristic by ship type**

Ship detection using SAR images has been studied for years. Classification, recognition, and other analyses of ships are of great importance for civil and military applications such as marine traffic safety, fishery control, and border surveillance. Some reviews of ship detection using the SAR imaging techniques have been well reported (Fingas and Brown 2001, Reed and Milgram 2002, Crisp 2004). However, the ship's SAR data set for detecting and classifying ships is limited; this can be solved by SAR simulation.

Multiple studies have focused on the method of analyzing the inverse synthetic aperture radar (ISAR) image using the EM Solver for a target modeled with CAD (Andersh, Moore et al. , Simpson, Galloway et al.). The simulated target models provide benefits such as target recognition, estimation, and performance evaluation of the object recognition capabilities.

In this study, we confirmed whether the SAR image produced by the simulator reflects the characteristics of the object. The simulation results were analyzed for three types of ships, as detailed in Table 3-2. Figure 3-4 shows the reference model of ship and the results obtained through the simulation. Figure 3-4(a) shows a cargo ship carrying containers. When the container is not loaded, the deck of the ship is flat; thus, the signal of the returned wavelength is weak. Therefore, as depicted in Figure 3-4(b), a strong signal is seen at the head and tail; on the contrary, the center has a

relatively smaller amplitude. Figure 3-4(c) shows a tanker ship carrying oil or gas. In the center of the ship, there are various facilities for storage. Therefore, as depicted in Figure 3-4(d), there is a stronger amplitude was obtained in the center of the ship. Figure 3-4(e) shows a fishing boat which is complicated in structure. Moreover, the image of the type of fishing ship that has a strong signal throughout the ship is shown in Figure 3-4(f).

**Table 3-2 Specification of Ships used in Simulation**

No	Ship Type	Length (m)	Width (m)	Height (m)	Weight (ton=1000kg)
1	Cargo	112	28	10	9215
2	Tanker	96	23	10	5659
3	Fishing Boat	90	20	10	3109

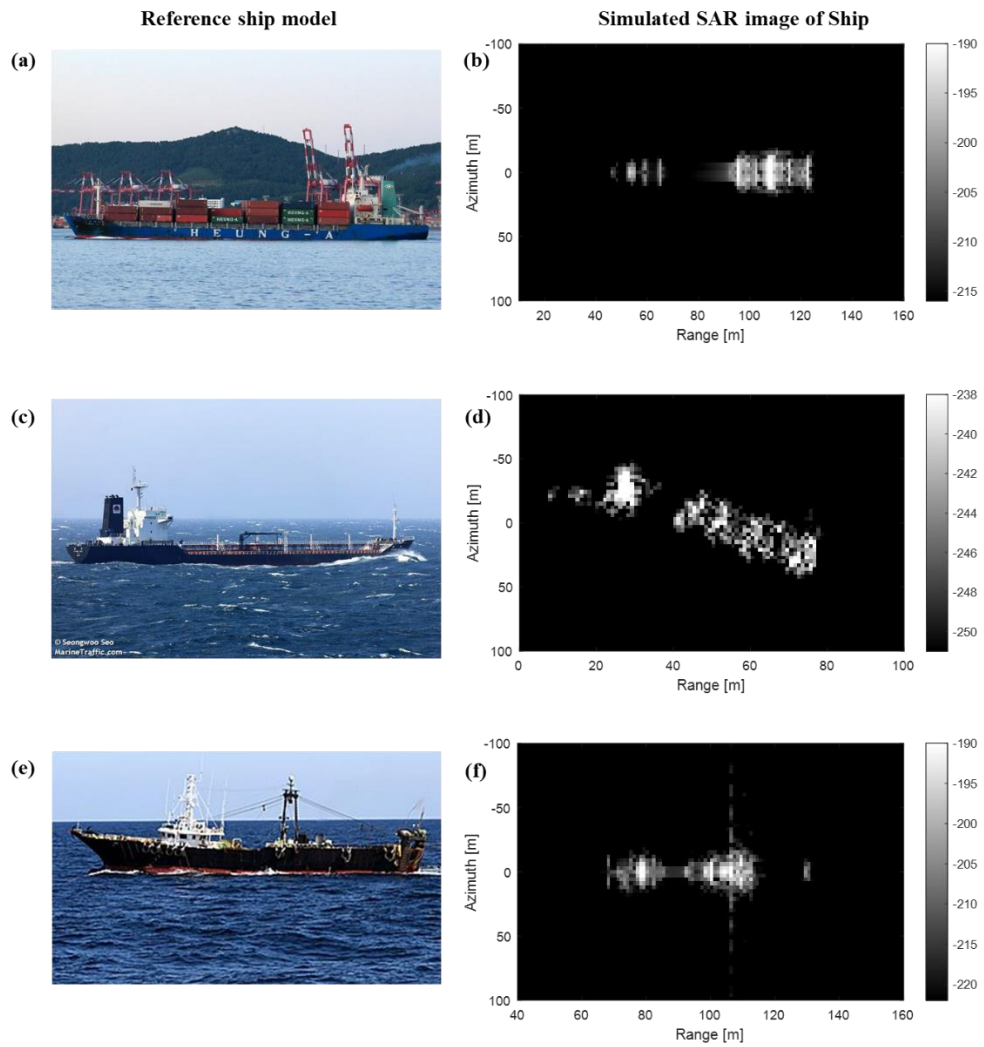


**Figure 3-4 (a), (c), and (e) - Reference ship models; (b), (d), and (f) – respective simulated SAR images of the ships.**

### **3.1.3 Analysis of rotation and polarization effect of ship**

As the resolution of SAR images increases, the details of deck configuration become more distinguishable, thus simplifying the ship classification (Liu and Jin 2017). For example, (Margarit, Mallorqui et al. 2006, Margarit, Mallorqui et al. 2009) implemented a SAR simulator to generate ship images based on simplified ship models.

For the same object, the scattering characteristics can be different based on its rotation and the viewing angle. The images rotated at 30, 45, and 60-degree intervals were analyzed for the cargo ship specified in Table 3-2. Figure 3-5 provides an overview of this experiment. Furthermore, images were acquired by rotating the vessel in the z-direction.

The raw data obtained from the simulation provides four polarization components: HH, HV, VH, and VV. Owing to the structural characteristics of the object, changes in polarization can be observed when the EM waves are reflects during its rotation. The experimental results are provided in Figures 3-6 through 3-9.

Summarizing these results, the stern control tower image shows a strong backscattering. This is because the structure of the control tower is large and complicated. On the other hand, since the center of the ship is a flat structure, the backscatter is weak; thus, it is hardly visible in the image. The part of an object closer to the antenna is reflected first; therefore, the area close to the antenna in the ship has

a stronger backscattering. HV and VH polarizations are weak in amplitude; however, they have different characteristics than those obtained from HH and VV polarization. In future, this polarization will be used to classify and detect ships.

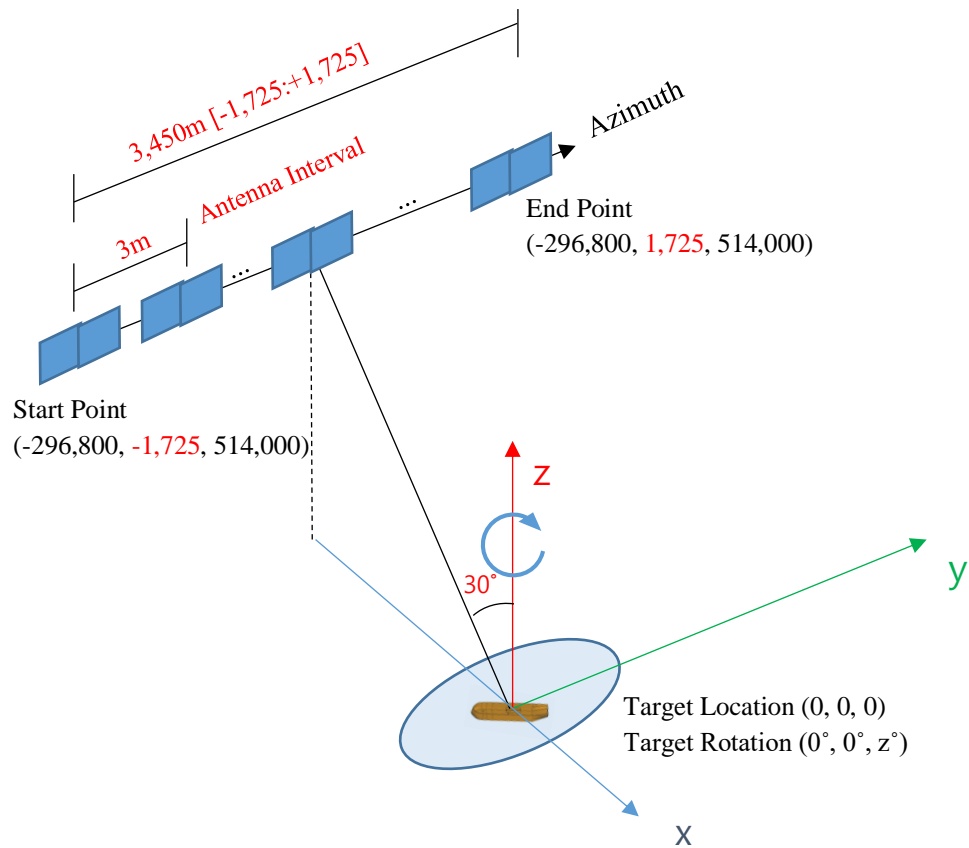


**Figure 3-5 Simulation overview of the rotation of the ship.**

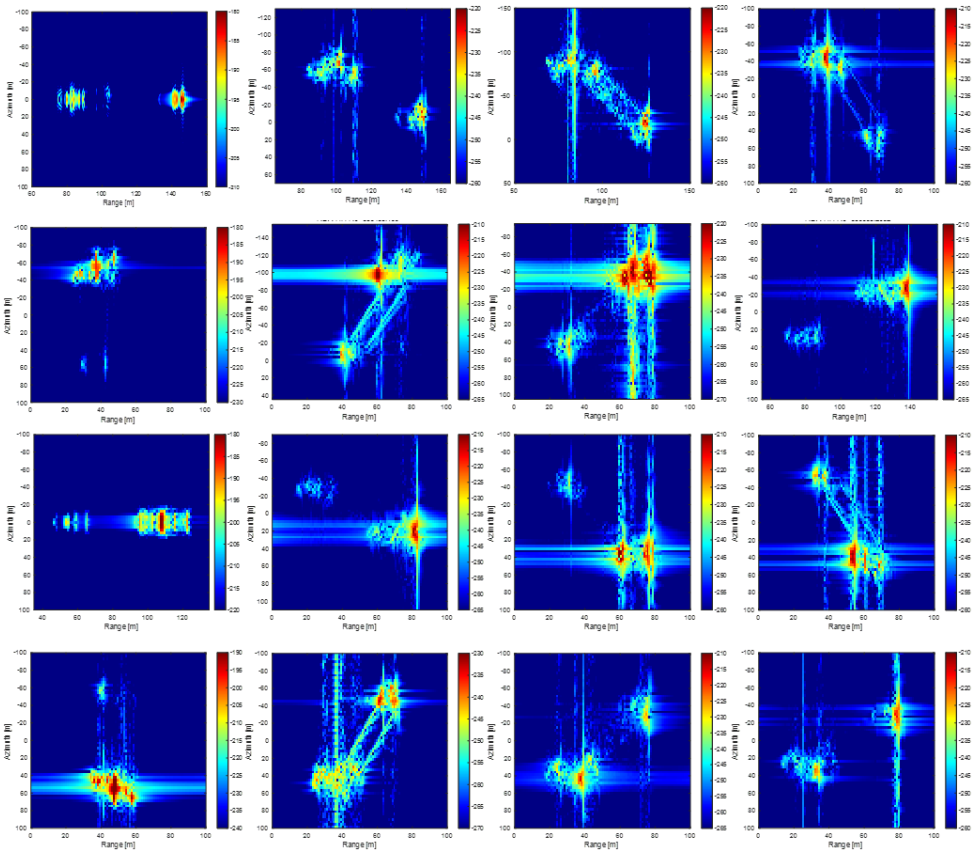


**Figure 3-6 HH polarized SAR simulation image for a rotating ship.**

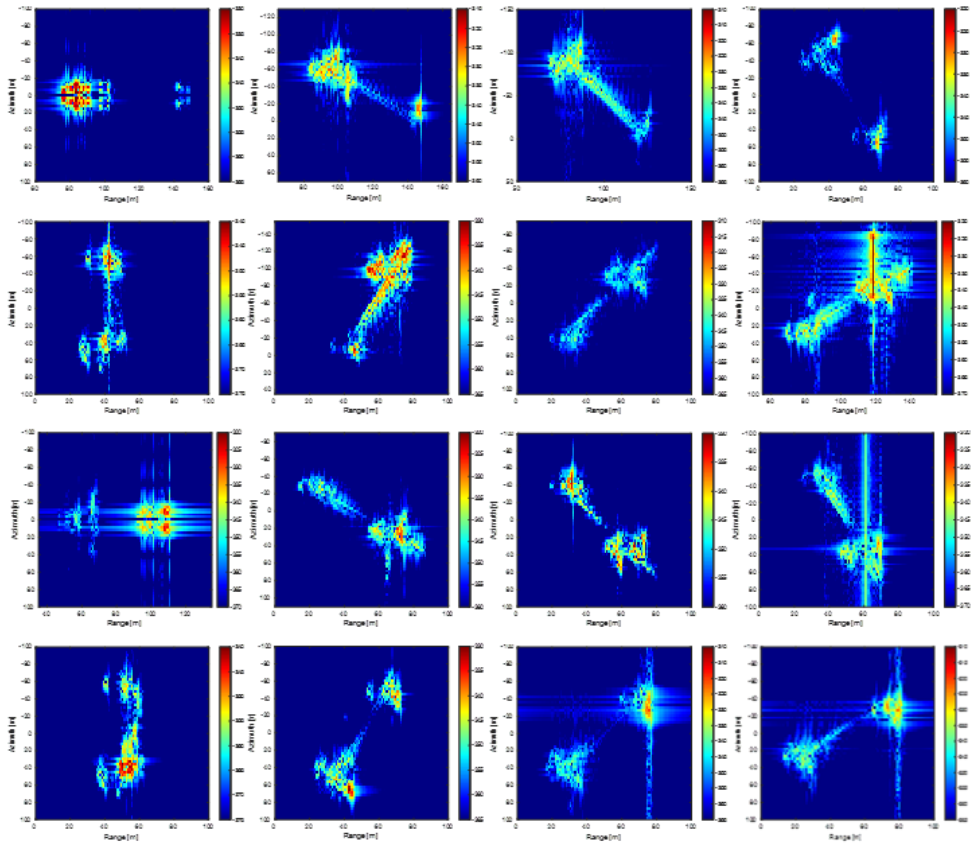


**Figure 3-7 VH polarized SAR simulation image for a rotating ship.**

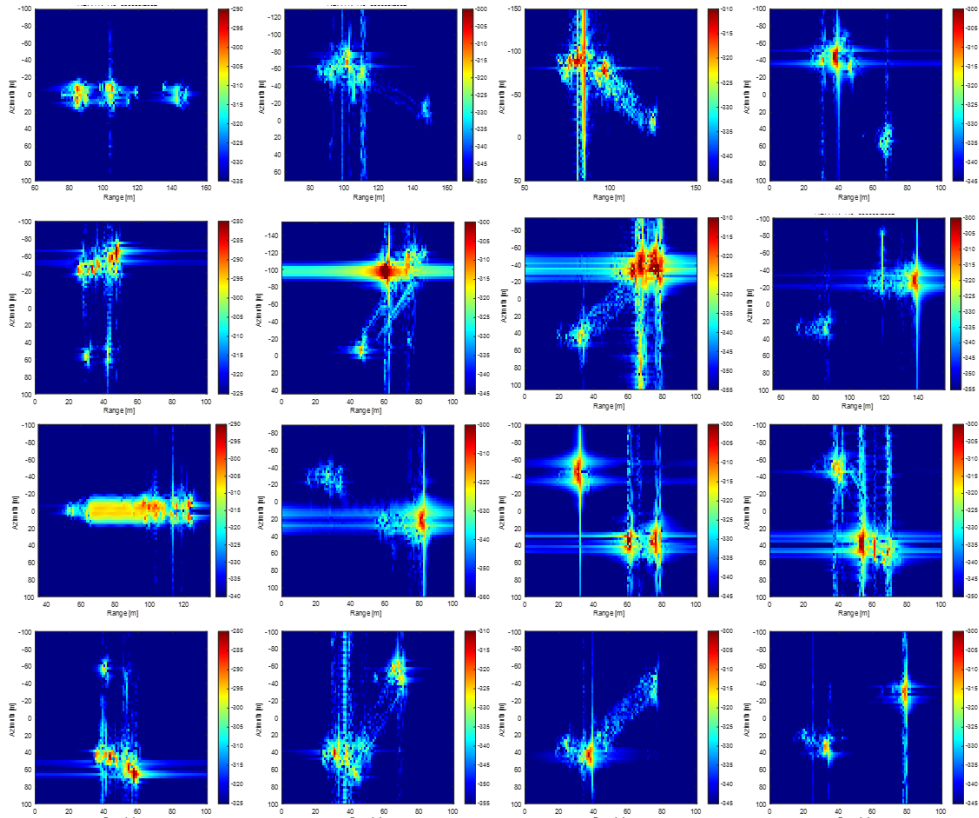


**Figure 3-8 HV polarized SAR simulation image for a rotating ship.**

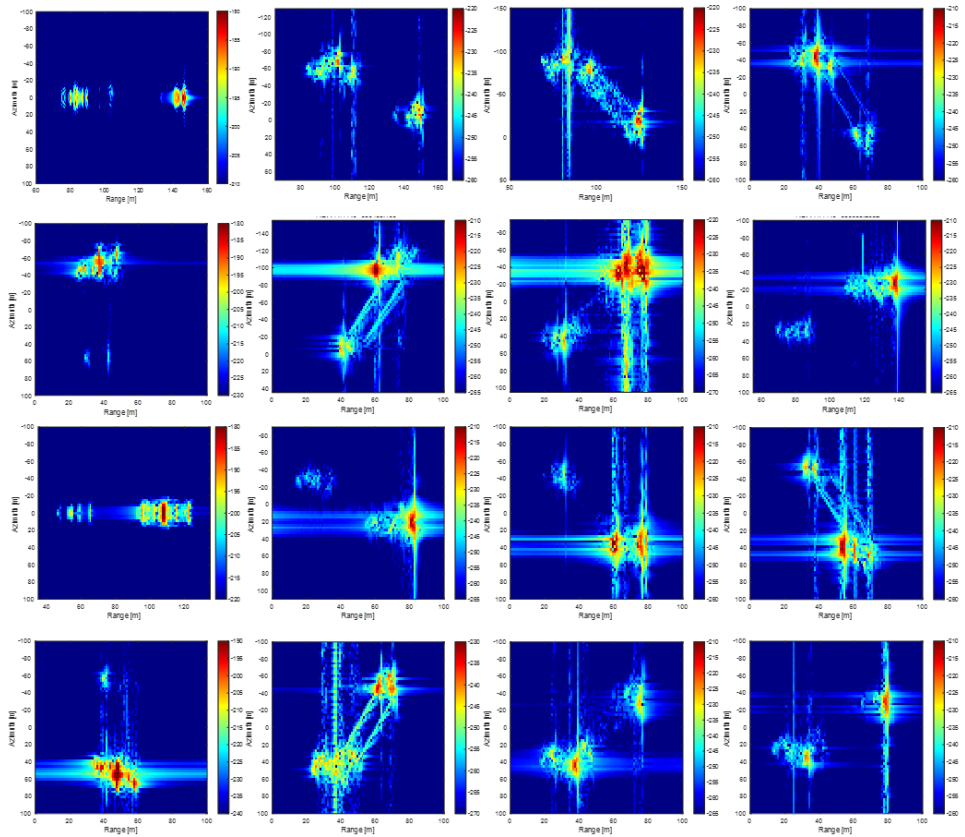


**Figure 3-9 VV polarized SAR simulation image for a rotating ship.**

### 3.2 Result of XTI-SAR simulation

In cross-track baseline InSAR (XTI-SAR), the height information  $z$  of an object is reflected in the phase  $\Delta\phi_{XTI}$ , as expressed by Eq. (21).

$$\Delta\phi_{XTI} = \frac{4 \pi B_c z}{\lambda R \sin\theta_{inc}} \quad (21)$$

The other values except height of the object,  $z$ , are constants. Therefore, the height of the object can be calculated using the XTI-SAR phase value. TanDEM-X uses this XTI-SAR method to create a global digital elevation model (DEM) that contains overall information of the earth with TerraSAR-X (Krieger, Moreira et al. 2007).

$$z_{max} = \frac{\lambda R \sin\theta_{inc}}{4 B_c} \quad (22)$$

According to Eq. (22), the larger the cross-track baseline, the more accurately the height of the object can be calculated. In this study, we simulated a range of cross-track baselines that could be included in the ATI mode of TanDEM-X.

An overview of the XTI-SAR experiment is illustrated in Figure 3-10. Without the along-track baseline, we created SAR images that changed the cross-track baseline component. The XTI-SAR result was then calculated using the interferogram.

Figure 3-10 provides the results of the simulation XTI-SAR. In this case, the distance between target and antenna,  $R$ , value of Eq. (22) gradually increases in the range direction and is called the flat-earth phase  $\Delta\phi_{\text{flat}}$ . This phase value must be removed, as expressed in Eq. (23), to obtain the correct phase value.

$$\Delta\phi_{\text{XTI}}^* = \Delta\phi_{\text{XTI}} - \Delta\phi_{\text{flat}} \quad (23)$$

Figures 3-11 (a) and (d) show the DEM results obtained using XTI-SAR when the cross-track baseline was 80 m and 100 m. By removing the flat phase, as depicted in Figures 3-11 (b) and (e), we obtain the corrected DEM, which is shown in Figures 3-11(c) and (f).

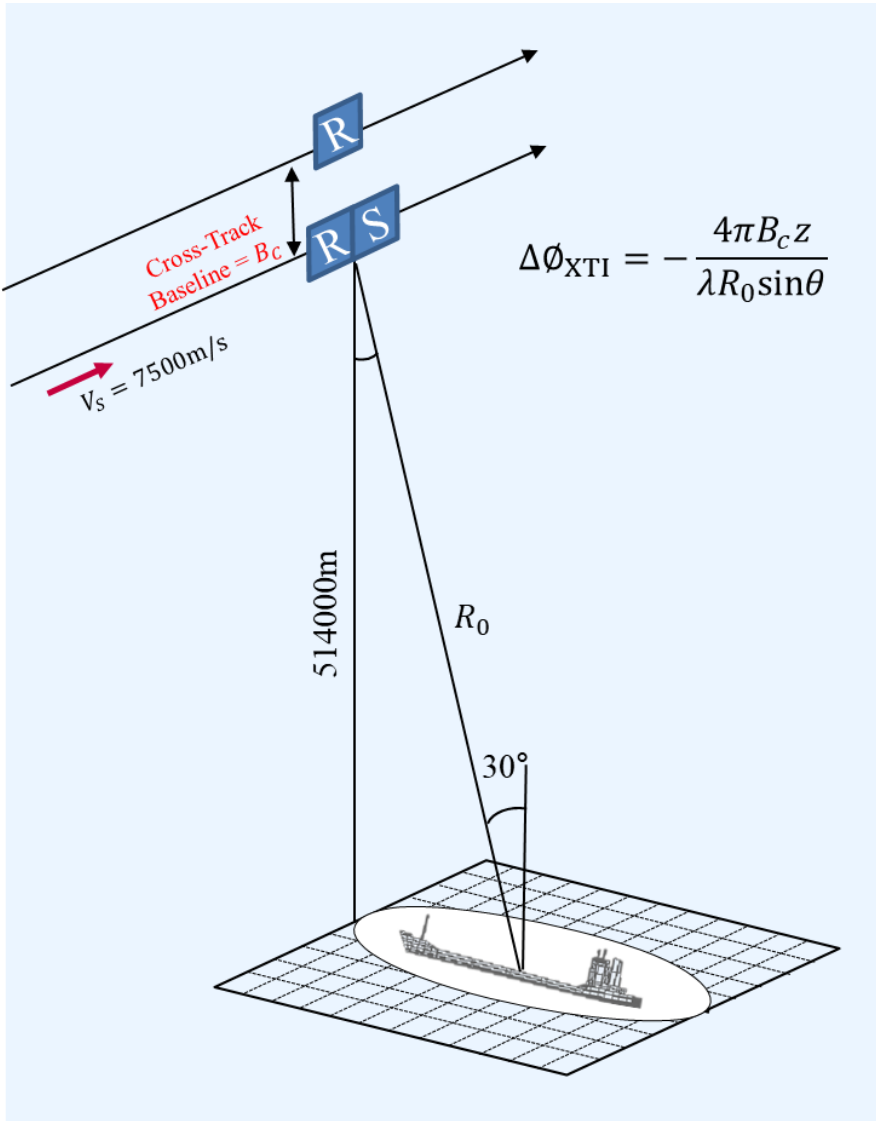


**Figure 3-10 Geometry of XTI-SAR simulation.**

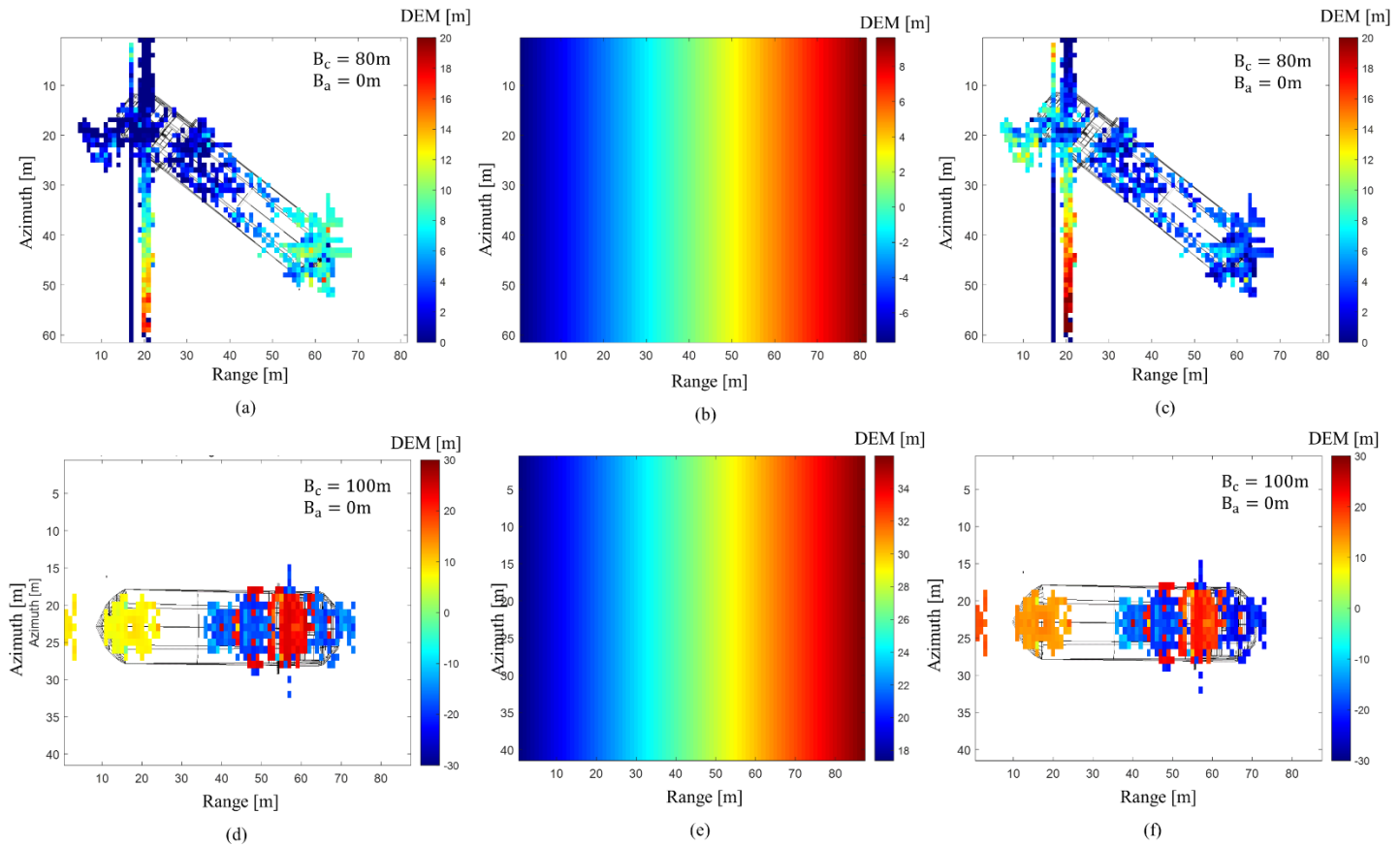


**Figure 3-11 For  $B_c = 80\text{ m}$ , (a) DEM result of ship model, (b) flat-Earth DEM, and (c) corrected DEM values. For  $B_c = 100\text{ m}$ , (d) DEM result of ship model, (e) flat-Earth DEM, and (f) corrected DEM values.**

### **3.3 Result of ATI-SAR simulation**

#### **3.3.1 Extraction of object velocity surface velocity**

Compression along-track interferometry is an InSAR method which can be used to obtain the required object velocities. Using the dual-channel SAR data obtained from highly center-separated phase centers on the platform, the ATI technology collects data from the center of the phase. the first image is called master and the second image is called slave. The schematic diagram of the ATI-SAR is shown in Figure 3-12. The SAR images formed from these two-phase centers feature a time-base line which corresponds to the time required for the platform to cover the offset distance between the tracks at the phase center. Therefore, the stationary elements in the rendered scene contribute equally to the two images whereas the moving objects in the scene represent phase shifts between the two images. As a result, the interference fringes formed from the two images represent the surface movement of the imaged scene (Chen 2004).

The phase difference is proportional to the Doppler shift of the backscattering signal; consequently, it is also proportional to the range velocity  $U_r$  of the scatterer (Kim, Moon et al. 2003) as expressed in Eq. (24).

$$\Delta\phi = \omega_D \Delta t = \frac{k_i B}{V_s} U_r = \frac{2\pi B}{\lambda_i V_s} U_r \quad (24)$$

where  $k_i$  and  $\lambda_i$  are the incident radar wave vector and wavelength, respectively.

$B$  is the baseline between the antennas.

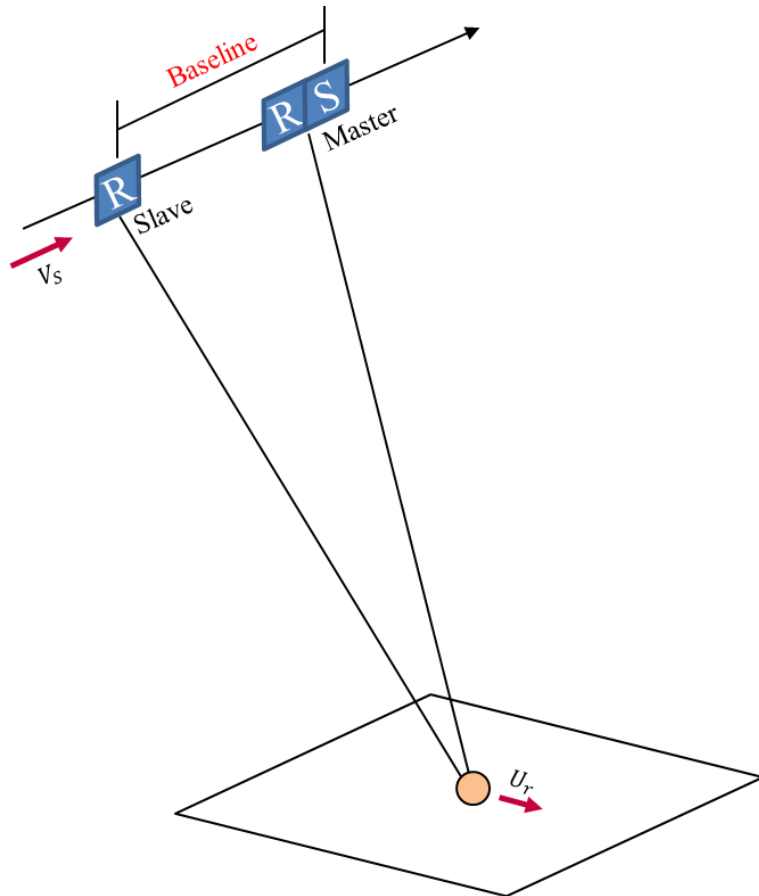


**Figure 3-12 Schematic geometry of the ATI-SAR simulation.**

### 3.3.2 ATI-SAR without cross-track baseline

The following is the ATI result of using an object as a ship. Based on the ATI when the ship was stopped, the results were compared with the ATI with the ship's speed. If the phase exceeds  $2\pi$ , phase wrapping occurs, which is difficult to analyze. Therefore, in this study, the ATI results were set to 0.5 m/s and 1.0 m/s, which are the speeds that do not exceed  $2\pi$  as expressed in Eq. (25).

$$V_s < \frac{2\pi B}{\lambda_i \Delta\phi_{ATI}} U_r \quad (25)$$

The experimental environment is illustrated in Figure 3-13. The baseline is set to 150m and the ship's speed is negative in the coordinate system because it is approaching towards the line of sight.

Figure 3-14 (a), (b), and (c) show the results of extracting the ship's speed from the ATI phase value when the ship's speed is 0 m/s, -0.5 m/s and -1.0 m/s. Generally, the ATI results match the speeds set in the simulation. Therefore, the EM-Solver seems to support the SAR-ATI. However, all the pixels of the ship image do not appear to have the same phase value. Although the object has a constant velocity, different phase information obtained suggests that the ATI value contains such information. As mentioned earlier, the height information of an object leads to a difference in the

radar delay time. Therefore, the phase value may be affected if the pixel has a complicated structure.

Figure 3-14 (a), (c), and (e) show the ATI results at 0 m/s, -0.5 m/s, and -1.0 m/s, respectively. Figure 3-14 (b), (d) and (f) depict the rates at which the ATI result values were extracted using Eq. (25). The calculated average speed values of these pixels are -0.0097 m/s, -0.4911 m/s, and -0.9994 m/s, respectively.

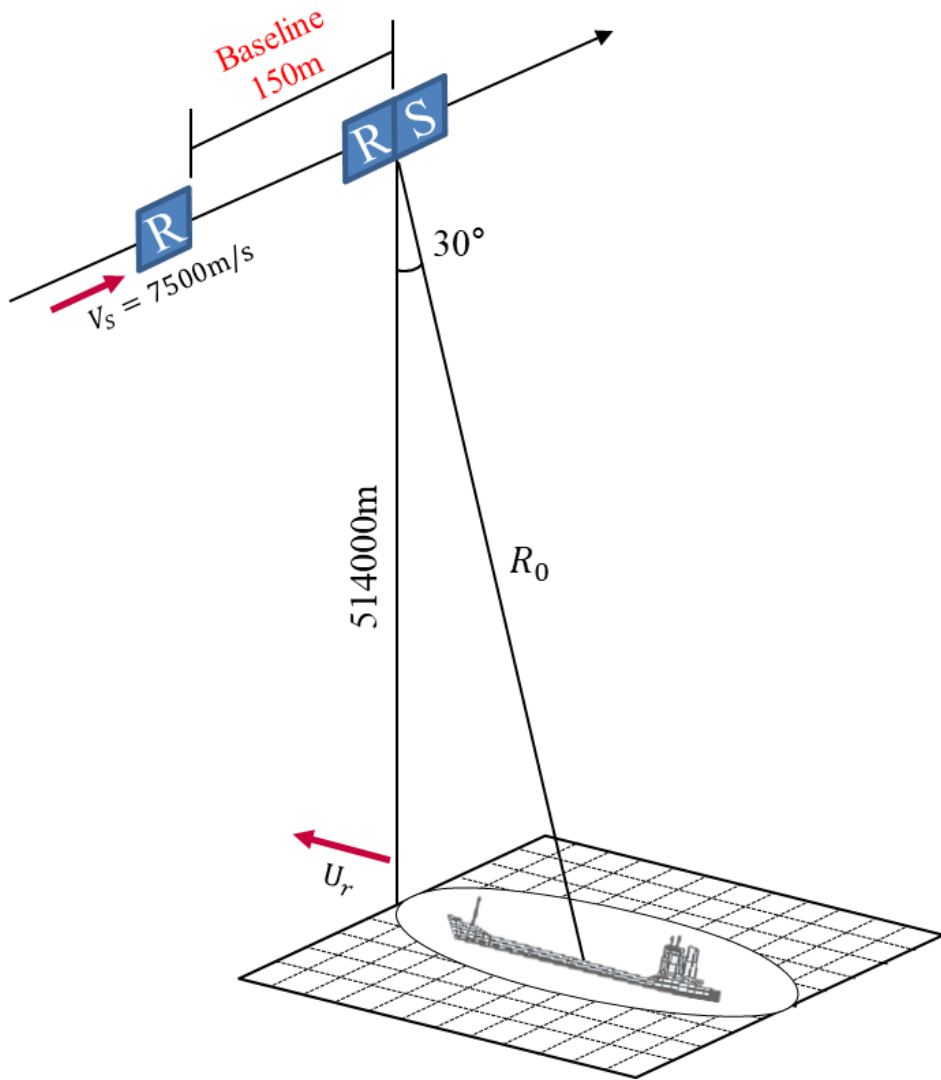
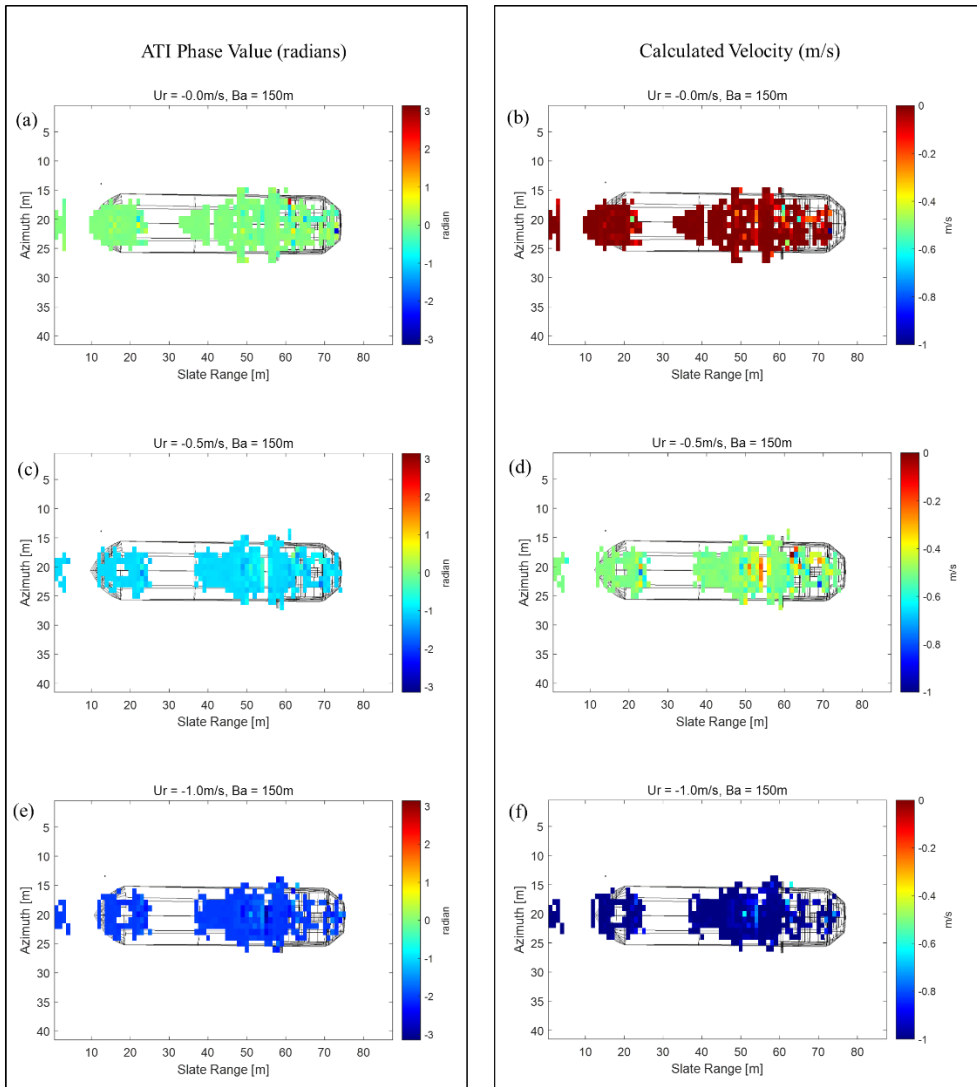


Figure 3-13 ATI-SAR simulation overview of the moving ship.



**Figure 3-14 Results of (a)  $U_r = 0\text{ m/s}$  (c)  $U_r = -0.5\text{ m/s}$  (e)  $U_r = -1.0\text{ m/s}$  ATI phase values. (b)  $U_r = 0\text{ m/s}$  (d)  $U_r = -0.5\text{ m/s}$  (f)  $U_r = -1.0\text{ m/s}$  calculated velocities.**

### 3.3.3 ATI-SAR with cross-track baseline

The study analyzed the results of ATI and the velocity with which the cross-track components were added in the ATI-SAR. The ATI phase values extracted from TanDEM-X do not harmonize. This can be because a cross track component was added.

The environment of the simulation is illustrated in Figure 3-15. The velocity  $U_r$  of the object was set to -0.5 m, and  $B_c$  values were set to 0 m, 2 m, 10 m, and 100 m, respectively. Figure 3-16 shows the simulation result, where Figure (a) provides the phase values when  $B_c$  is 0 m, Figure (b) is the result of velocity extraction using Figure (a), and the average velocity of the pixels is -0.493 m/s. Moreover, Figure (d) is the velocity extracted using the data in Figure (c), which provides the resultant phase values when  $B_c$  is 2 m and the average value of velocity in each pixel is -0.242 m/s. Figure (f) is the velocity extracted using the data from Figure (e), which gives the resultant phase values when  $B_c$  is 10 m and the average value of velocity in each pixel is -0.104 m/s. Finally, Figure (h) is the velocity extracted using the data from Figure (g), which is the result of phase values when  $B_c$  is 100 m and the average value of each pixel is -0.409 m/s. When the cross-track baseline is 2 m, the speed is different from the expected theoretical value; however, the overall value is uniform. On the other hand, if the cross-track baseline is more than 10 m, the overall phase value is heterogeneous. It is considered that the phase value of the height of the object by the cross-track baseline has a larger weightage in the InSAR result.

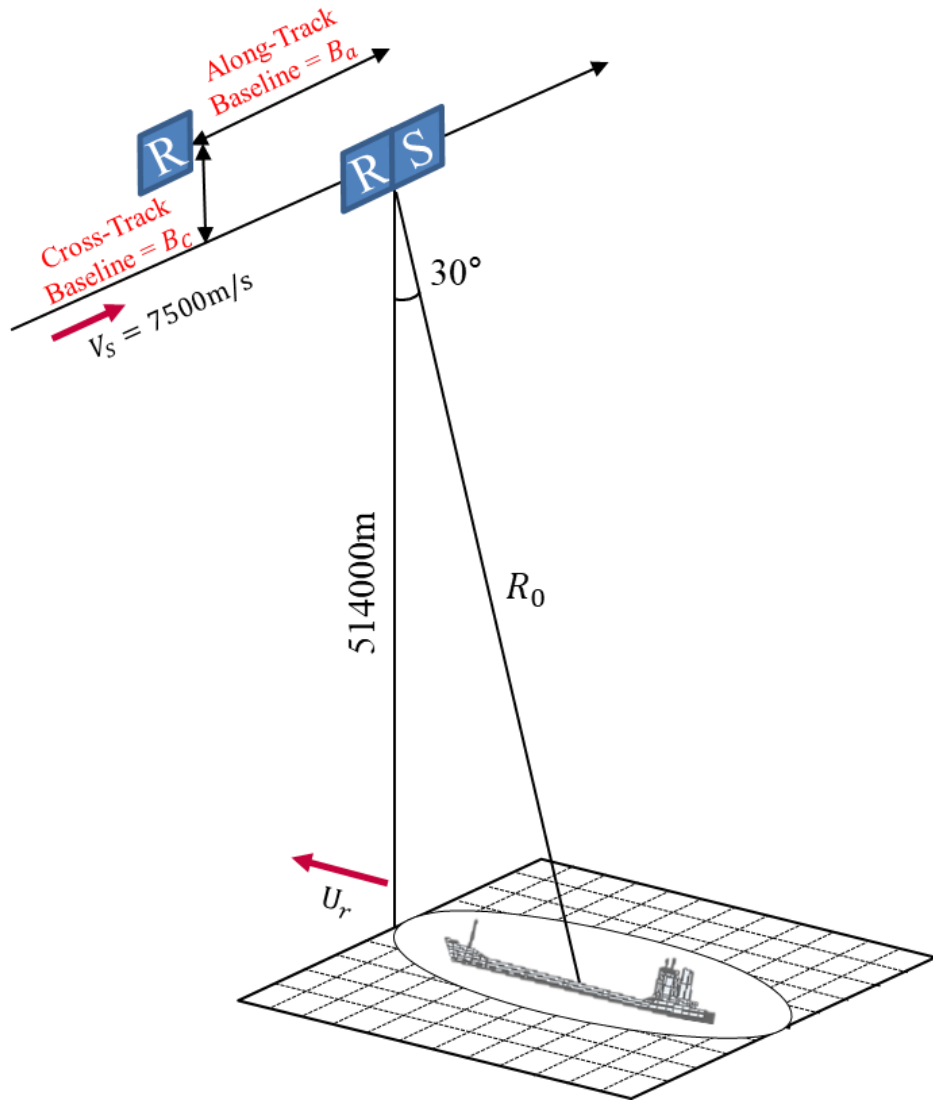
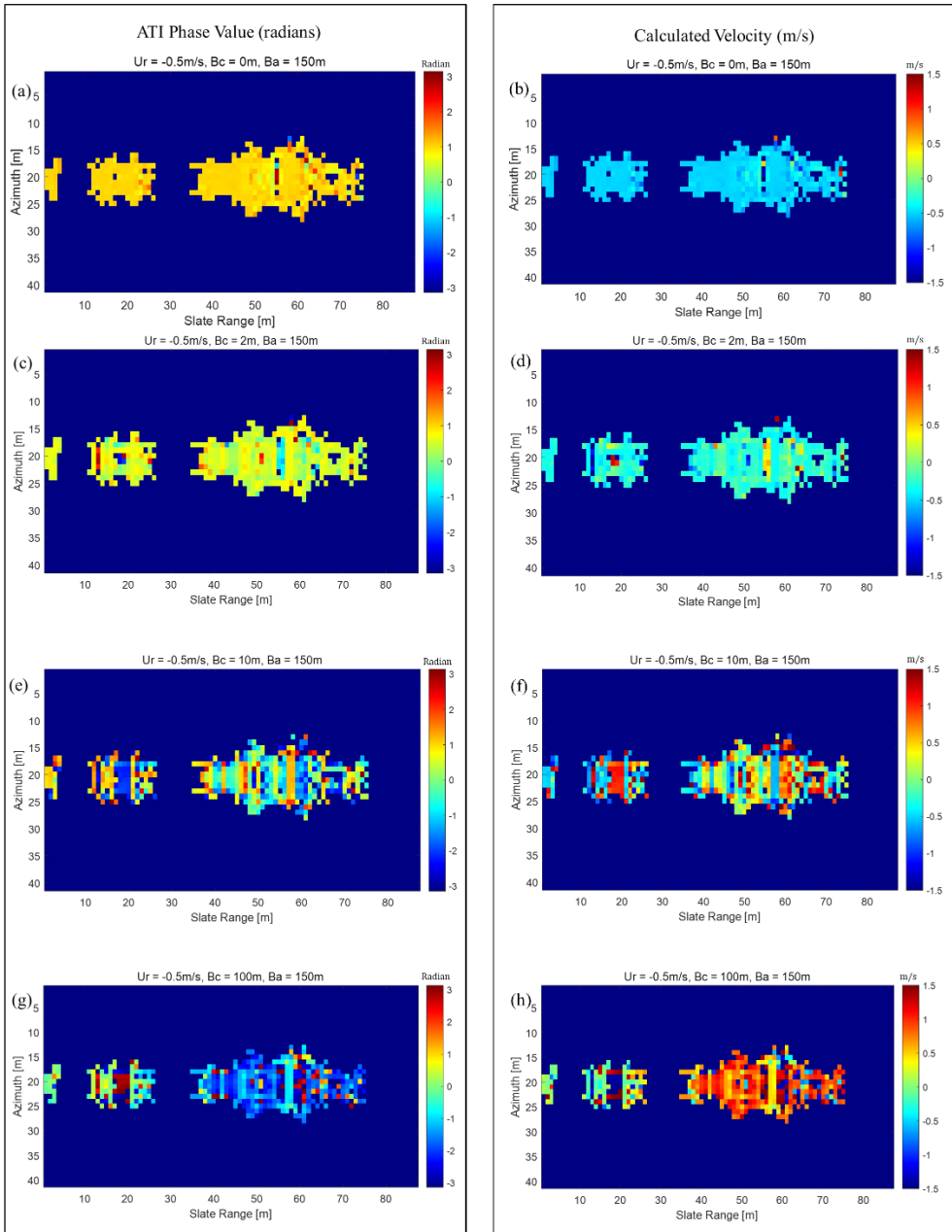


Figure 3-15 ATI-SAR simulation with cross-track baseline.



**Figure 3-16 (a)  $B_c = 0 \text{ m}$  (c)  $B_c = 2 \text{ m}$  (e)  $B_c = 10 \text{ m}$  (g)  $B_c = 100 \text{ m}$ , ATI phase values. (b)  $B_c = 0 \text{ m}$  (d)  $B_c = 2 \text{ m}$  (f)  $B_c = 10 \text{ m}$  (h)  $B_c = 100 \text{ m}$ , calculated velocities.**

### 3.3.4 Velocity extraction from ATI- and XTI-SAR

From the previous results, it was confirmed that the addition of cross-track components affects the ATI phase value. In the ATI-SAR, the effect of the cross-track component on the results is given by Eq. (26) and it is confirmed that an accurate velocity extraction is difficult.

$$\Delta\phi_{\text{Total}} = \Delta\phi_{\text{XTI}} + \Delta\phi_{\text{ATI}} \quad (26)$$

To extract the precise velocity to interferogram  $\Delta\phi_{\text{Total}}$ , the phase value of InSAR  $\phi_{\text{ATI}}$ , calculated only with cross-track, can be subtracted from the result. The interferogram provided a phase of  $\Delta\phi_{\text{XTI}}$ , using only the cross-track components, to extract the accurate speeds.

The obtained results were then subtracted by subtracting the corresponding XTI-SAR phase component from the ATI results with the cross-track added. Figure 3-17 (a) shows the ATI-SAR with the added cross-track. Figure 3-17 (d) is the generated XTI-SAR phase result and Figure 3-17 (e) is the result corrected using Eq. (26). Comparing this with Figure 3-17 (c), which does not include cross-track, it has the same phase value. This indicates that it is possible to calibrate the phase value using the ship's height information.

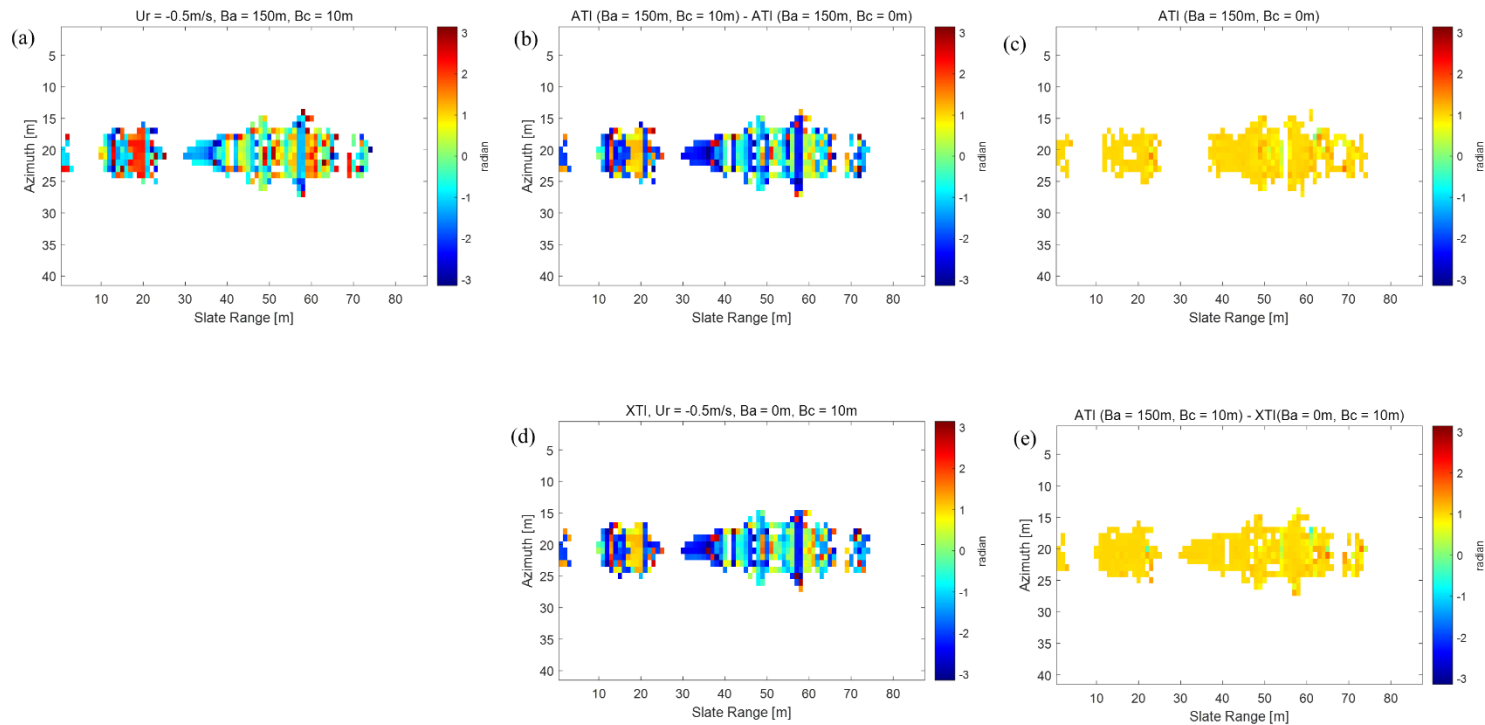


**Figure 3-17** For a ship velocity of  $-0.5\text{ m/s}$ , (a) ATI-SAR result with cross-track baseline ( $B_A = 150\text{ m}$ ,  $B_C = 10\text{ m}$ ), (b) residual phase (c)–(a), (c) ATI-SAR result ( $B_A = 150\text{ m}$ ,  $B_C = 0\text{ m}$ ), (d) XTI-SAR result ( $B_A = 0\text{ m}$ ,  $B_C = 10\text{ m}$ ), and (e) adjusted ATI-SAR results of (a)–(d).

### 3.3.5 ATI-SAR results for moving ship

The phase information in ATI-SAR image may include not only the velocity of the object, but also the movement caused by other elements such as waves. In this study, we analyzed the changes that occur when a ship's height changes due to waves. When the location of the antenna is  $U(X, Y, Z)$  and the motion of the object is  $f(x, y, z)$ , the delay time  $t_d$  is expressed by Eq. (27).

$$t_d = \frac{2}{c} \sqrt{(f(x) - U(X))^2 + (f(x) - U(X))^2 + (f(x) - U(X))^2} \quad (27)$$

Figure 3-18 illustrates a simulation of the ship's movement. In addition to the linear movement of the object, the image can be also created by reflection from the rotating elements. Figure 3-19 depicts the simulation results when the ship moves up and down in the  $T_z$  direction due to waves when the velocity of the object is constant at (b) 0 m/s, (c) 0.1 m/s, and (d) -1.1 m/s in the  $T_x$  direction. The pixel values of each result have similar values in general; however, the average speed is constantly changed by the speed difference in the  $T_z$  direction.

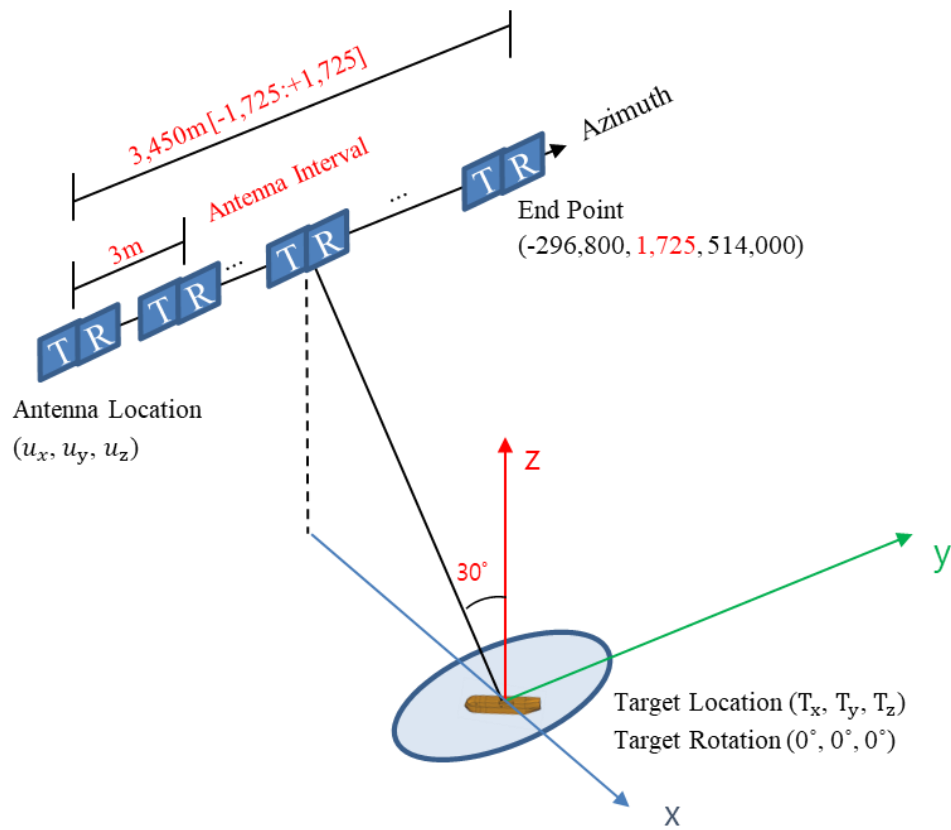


**Figure 3-18 Simulation overview of the ship movement.**

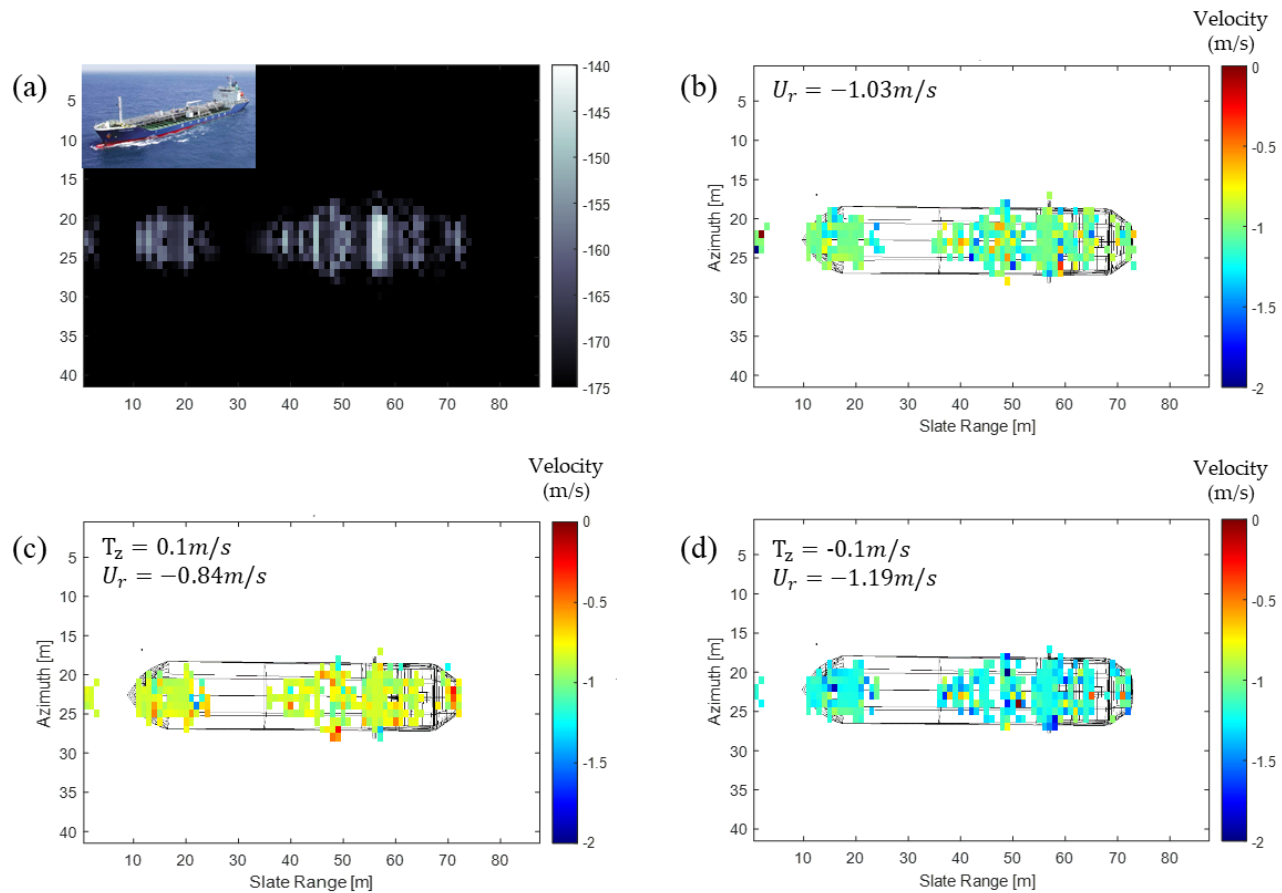


**Figure 3-19 (a) Simulation SAR results; velocity extraction results using ATI-SAR when (b),  $T_z = 0 \text{ m/s}$  (c)  $T_z = 0.1 \text{ m/s}$  and (d)  $T_z = -0.1 \text{ m/s}$ .**

### 3.4 Analysis of phase error in Korean Strait

This study analyzed the results of ATI and the velocity with which the cross-track components were added in ATI-SAR. As shown in Figure 3-20(a) and (b), along-track and perpendicular baselines differed by latitude in the ATI mode of Tandem-X from June 10, 2011 to August 16, 2012. This is a result of the spiral orbit between the two satellites. Therefore, a perpendicular baseline in the ATI mode is indispensable. As a result, the height of the object corresponding to Eq. (24) is reflected in the ATI phase. Especially in the case of Korea's oceans, cross-track components are inevitably included in the ATI results. In this study, based on the previous results, when the ship's speed is extracted using TanDEM-X's ATI in Korean strait, we analyzed the cross-track phase component because of the height difference of ship.

In Korean strait, cross-track is inevitably included in the ATI data obtained using TanDEM-X. As a result, the ATI data may be inaccurate for objects with heterogeneous heights, such as ships. Figure 3-20 (c), (d), and (e) depict the results of calculating the speed error due to the perpendicular baseline calculated based on the orbit of the period. These results imply that the larger the difference in height of the objects and the larger the vertical baseline, the greater the error that can occur when the ATI method is implemented. The perpendicular baseline while descending and ascending in Korean strait is shown in Table 3-3. In general, it can be confirmed that the cross-track component is larger while ascending. After this, the phase information is calculated using Eq. (21), considering the largest height difference  $\Delta z$  of 15 m in a

cargo ship, as detailed in Table 3-2. If the height difference of the object is 15 m, the phase value added to the ATI result for each cross-track component is provided in Table 3-3 below. In the ascending mode, because the cross-track component is long, a large value over  $\pi$  is added to the phase value. Therefore, using the ascending mode can make it difficult to extract the velocity of the object with the height difference. On the other hand, in the descending mode, the phase value due to the height difference exists; however, because it is relatively small, correcting it may help in extracting an accurate speed.

**Table 3-3 Perpendicular baseline of Korean Strait in TanDEM-X.**

Velocity error value	Look angle (deg)	Latitude (deg)	Ascending		Descending	
			Perpendicular Baseline (m)	$\Delta z = 15$ m, $\Delta\phi_{XTI}$ (rad)	Perpendicular Baseline (m)	$\Delta z = 15$ m, $\Delta\phi_{XTI}$ (radians)
Minimum	43.2	38	245	3.080	Minimum	43.2
Maximum	28.7	28.7	255	3.206	Maximum	28.7

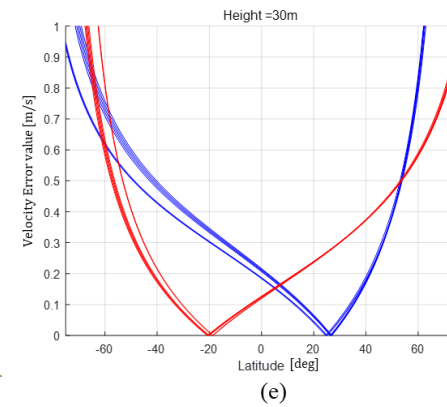
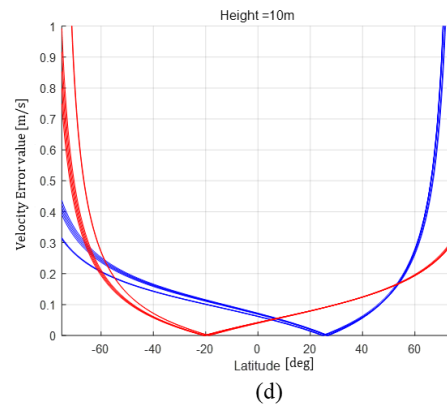
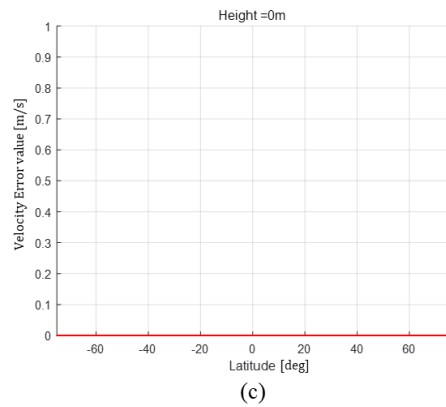
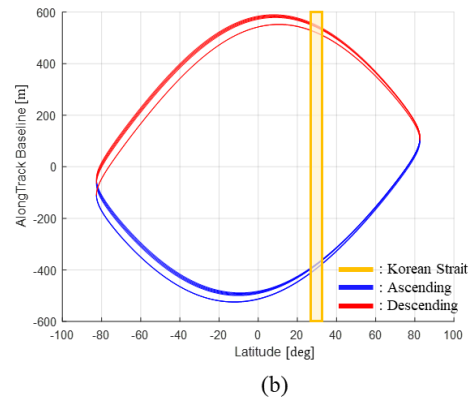
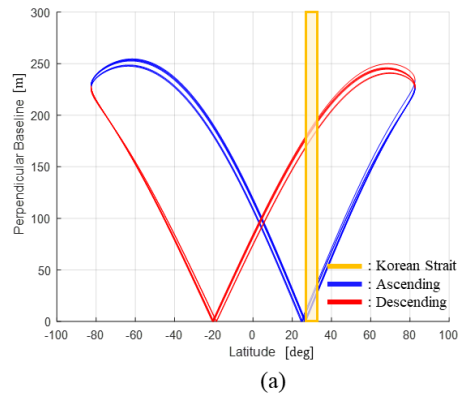


**Figure 3-20 (a) TanDEM-X perpendicular and (b) along-track baseline for different latitudes for the bistatic short baseline phase from June 10, 2011 to August 16, 2012. Velocity error value depending on latitude when height difference is (c) 0 m, (d) 10 m, and (e) 30 m.**

## **Chapter 4.**

### **Conclusions**

In an environment like TerraSAR-X and TanDEM-X, raw data for point targets were generated using the EM Simulation. Based on the generated SAR raw data, ATI components were extracted. Moreover, simulations were performed in a controlled environment to obtain accurate baseline settings and location of the object. To extract velocity and height of the ship, we created two SAR images using the EM simulator, which digitized the analysis target with CAD. Furthermore, we analyzed the actual satellite data based on the obtained simulation data.

Using simulated SAR images, the following studies were conducted:

1. Characteristic of Simulation SAR (ship type, rotation of ship and polarization)
2. Cross-Track Interferometric SAR
3. Along-Track baseline Interferometric SAR
4. ATI-SAR Results with Movement of Ship

We analyzed the factors that influenced the phase value in the ATI-SAR environment. The simulations showed that cross tracks affect the phase value in the ATI mode of the TDX. As a result, the height of the object was considered to affect the ATI velocity extraction. The simulation also confirmed that the ship's acceleration and movement affected the phase in the ATI mode. Future works will use a simulator to quantitatively analyze the effects of these factors.

In addition, we will conduct a study on the SAR system with both cross-track and

along-track using the InSAR simulation with CAD. The SAR system aims to identify the object, calculate the exact velocity, and classify it by using the DEM of the artificial object, which is calculated by simulation.

## 국문 요약문

선박 속도 모니터링은 해상 교통 모니터링 및 재해 예방과 관련된 중요한 작업 중 하나이다. SAR는 날씨, 낮 또는 밤에 관계없이 모니터링 할 수 있기 때문에 이에 적합한 시스템이다. ATI-SAR은 표면 속도를 추출하는 InSAR 기술 중 하나로 Along-track의 길이에 따라 빙하와 같은 속도가 느린 물체에서부터 선박과 같은 빠른 속도의 물체에 이르기까지 ATI 데이터를 사용하여 속도를 측정할 수 있다.

TerraSAR-X와 TanDEM-X 위성은 X-band를 사용하여 고해상도 SAR 이미지를 얻으므로 이 데이터를 통해 ATI-SAR 기법을 사용하면 표면 물체 속도를 보다 정확하게 계산할 수 있다. 한편, 선박과 같은 물체의 경우 영상에 단일 물체가 여러 픽셀에 걸쳐 나오는데 ATI 결과값에서 물체의 위상 값은 물체의 속도를 나타내기 때문에 모든 픽셀의 값이 같아야 한다. 그러나 ATI-SAR 결과로 계산된 일부 선박 속도는 각 픽셀마다 다르게 나타난다. 이는 ATI 기법으로 추출된 물체의 오차 값을 야기하고 ATI 기법의 신뢰를 떨어뜨리게 된다. 오차의 원인은 선박의 3차원 구조와 가속 및 흔들림 등에 인한 것으로 추정되지만 실제 환경에서는 자연환경에 의한 다양한 요인이 결과에 반영되므로 이러한 원인을 확인하기가 쉽지 않다.

본 연구에서는 EM 시뮬레이터를 사용하여 ATI 결과에 영향을 줄 수

있는 요인들을 분석했다. EM 시뮬레이터는 컨트롤 되는 환경에서 원하는 변수로 시뮬레이션을 할 수 있기 때문에 분석이 용이하기 때문이다. 시뮬레이터는 객체의 3 차원 특성을 반영할 수 있는 선박 모델의 CAD 파일을 사용했으며 선박에서 발생할 수 있는 움직임과 관련된 요소를 직관적으로 추가할 수 있는 직교 좌표계 환경을 사용했다. 시뮬레이션으로 생성된 원시 SAR 데이터를 영상 압축 알고리즘을 사용해 SAR 영상으로 만들었으며 물체의 입체적 구조와 움직임 등을 반영해 InSAR 결과물을 만들 수 있었다.

시뮬레이션 SAR 자료는 실제 SAR 자료와 같은 특성을 가지고 있으며 InSAR 기법인 XTI-SAR와 ATI-SAR의 결과 역시 이론적인 값과 같은 것을 확인했다. 이를 통해 선박에서 일어날 수 있는 움직임과 선박의 3차원 특성을 반영한 요소들을 InSAR 결과에 반영하고 위상 값에 영향을 주는 것을 검증했다. 이는 과거 연구 방법으로는 직접적으로 확인하기 힘든 사항이었다.

추후, 해당 시뮬레이션을 이용하여 정밀한 ATI-SAR 결과물 분석, ATI-SAR 위성의 시스템 설계, cross-track 과 along-track 기준선이 포함된 InSAR 결과물에서 인공적 구조물에 대한 표적 식별 및 속도 추출 등 다양한 분야에 적용될 수 있을 것으로 예상된다.

**주요어 :** SAR, EM Simulator, ATI-SAR, Velocity estimation

## **Bibliography**

Andersh, D., J. Moore, S. Kosanovich, D. Kapp, R. Bhalla, R. Kipp, T. Courtney, A. Nolan, F. German and J. Cook Xpatch 4: The next generation in high frequency electromagnetic modeling and simulation software, IEEE.

Chen, C. W. (2004). Performance assessment of along-track interferometry for detecting ground moving targets. Proceedings of the 2004 IEEE Radar Conference (IEEE Cat. No. 04CH37509), IEEE.

Crisp, D. J. (2004). The state-of-the-art in ship detection in synthetic aperture radar imagery, Defence Science And Technology Organisation Salisbury (Australia) Info ....

Cumming, I. G. and F. H. J. B. Wong, MA, USA: Artech House (2005). "Digital Processing of Synthetic Aperture Radar Data: Algorithms and Implementation [With CDROM](Artech House Remote Sensing Library)."

Duk-jin, K., W. M. Moon, D. Moller and D. A. Imel (2003). "Measurements of ocean surface waves and currents using L- and C-band along-track interferometric SAR." IEEE Transactions on Geoscience and Remote Sensing **41**(12): 2821-2832.

Ferdous, M. S., P. McGuire, D. Power, T. Johnson and M. Collins (2018). "A Comparison of Numerically Modelled Iceberg Backscatter Signatures with Sentinel-1 C-Band Synthetic Aperture Radar Acquisitions." Canadian Journal of Remote

Sensing **44**(3): 232-242.

Fingas, M. F. and C. E. Brown (2001). "Review of ship detection from airborne platforms." *Canadian journal of remote sensing* **27**(4): 379-385.

García Díaz, J. L. (2015). "Diseño e implementación de un sistema de simulación electromagnética en remoto aplicado al análisis de antenas."

Hanssen, R. F. (2001). *Radar interferometry: data interpretation and error analysis*, Springer Science & Business Media.

Ishimaru, A. (1978). *Wave propagation and scattering in random media*, Academic press New York.

Kang, K. and D. Kim (2019). "Ship Velocity Estimation From Ship Wakes Detected Using Convolutional Neural Networks." *IEEE Journal of Selected Topics in Applied Earth Observations and Remote Sensing*: 1-10.

Keller, J. B. (1962). "Geometrical Theory of Diffraction\*." *Journal of the Optical Society of America* **52**(2): 116-130.

Kim, D.-j., J. Jung, K.-m. Kang, S. H. Kim, Z. Xu, S. Hensley, A. Swan and M. J. S. Duersch (2015). "Development of a cost-effective airborne remote sensing system for coastal monitoring." **15**(10): 25366-25384.

Kim, D.-j., W. M. Moon, D. Moller and D. A. Imel (2003). "Measurements of ocean surface waves and currents using L-and C-band along-track interferometric SAR."

IEEE Transactions on Geoscience and Remote Sensing **41**(12): 2821-2832.

Kim, K.-T., D.-K. Seo and H.-T. Kim (2005). "Efficient classification of ISAR images." IEEE Transactions on Antennas and Propagation **53**(5): 1611-1621.

Kim, S. and D.-j. Kim (2017). "Combined usage of TanDEM-X and Cryosat-2 for generating a high resolution digital elevation model of fast moving ice stream and its application in grounding line estimation." Remote Sensing **9**(2): 176.

Krieger, G., A. Moreira, H. Fiedler, I. Hajnsek, M. Werner, M. Younis and M. Zink (2007). "TanDEM-X: A Satellite Formation for High-Resolution SAR Interferometry." IEEE Transactions on Geoscience and Remote Sensing **45**(11): 3317-3341.

Liu, P. and Y.-Q. Jin (2017). "A study of ship rotation effects on SAR image." IEEE Transactions on Geoscience and Remote Sensing **55**(6): 3132-3144.

Margarit, G., J. J. Mallorqui, J. Fortuny-Guasch and C. López-Martínez (2009). "Phenomenological vessel scattering study based on simulated inverse SAR imagery." IEEE Transactions on Geoscience and Remote Sensing **47**(4): 1212-1223.

Margarit, G., J. J. Mallorqui, J. M. Rius and J. Sanz-Marcos (2006). "On the usage of GRECOSAR, an orbital polarimetric SAR simulator of complex targets, to vessel classification studies." IEEE Transactions on Geoscience and Remote Sensing **44**(12): 3517-3526.

Menon, M. M., E. R. Boudreau and P. J. Kolodzy (1993). "An automatic ship classification system for ISAR imagery." *The Lincoln Laboratory Journal* **6**(2): 289-308.

Meyer, F., S. Hinz, R. Müller, G. Palubinskas, C. Laux and H. Runge (2007). "Towards traffic monitoring with TerraSAR-X." *Canadian Journal of Remote Sensing* **33**(1): 39-51.

Moreno, J., G. Caballero, C. Delgado, E. Garcia, L. Lozano, I. Gonzalez and F. Catedra (2013). New modules and features introduced in NEWFASANT. 2013 7th European Conference on Antennas and Propagation (EuCAP), IEEE.

Nguyen, L., M. Ressler, D. Wong and M. Soumekh (2004). Enhancement of backprojection SAR imagery using digital spotlighting preprocessing. Proceedings of the 2004 IEEE Radar Conference (IEEE Cat. No.04CH37509).

Ozdemir, C. (2012). Inverse synthetic aperture radar imaging with MATLAB algorithms, John Wiley & Sons.

Reed, A. M. and J. H. Milgram (2002). "SHIP WAKES AND THEIR RADAR IMAGES." *Annual Review of Fluid Mechanics* **34**(1): 469-502.

Romeiser, R., S. Suchandt, H. Runge, U. Steinbrecher, S. J. I. T. o. G. Grunler and R. Sensing (2010). "First analysis of TerraSAR-X along-track InSAR-derived current fields." **48**(2): 820-829.

Romero, G., y González, I. (2010). "Diseño e implementación de una plataforma avanzada de ejecución remota vía web: módulos MONURBS y POGCROS." Trabajo Fin de Carrera de Ingeniería en Informática de la Universidad de Alcalá: 14-19.

Simpson, S. H. W., P. Galloway and M. Harman Applications of epsilon to a radar signature prediction and analysis tool.

Soumekh, M. (1999). Synthetic aperture radar signal processing, New York: Wiley.

Timoteo, L. (2011). "NewFasant, una EBT puntera en el diseño y medición de antenas." Diario Digital de la Universidad de Alcalá.